

CHIMIE NOUVELLE

LA REVUE DE CONTACT DE LA **SOCIÉTÉ ROYALE DE CHIMIE**

40^{ème} année - novembre 2022



CN 140

<h3>Chimie des surfaces</h3> <p>X4C - Innovative surface functionalization for efficient diagnostic tests</p> <p>A. MATTIUZZI, A.-M. BAUDUIN, L. TROIAN-GAUTIER, I. JABIN</p>	1
<h3>catalyse photorédox</h3> <p>Activation de Liaisons Carbone – Azote et Utilisation des Sels d'Ammonium comme Précurseurs de Radicaux</p> <p>C. THEUNISSEN</p>	8
<h3>cellules solaires organomoléculaires</h3> <p>A Joint Theoretical and Experimental Characterization of the Rising Star Y6 Acceptor in Organic Solar Cells – From Molecules to Devices</p> <p>F. REGNIER, A. RILLAERTS, V. LEMAUR, P. VIVILLE, J. CORNIL</p>	17

Directeurs de rédaction

Bernard Mahieu
UCLouvain, Ecole de Chimie
Place Pasteur, 1
Boîte L4.01.07
1348 Louvain-la-Neuve
bernard.mahieu@uclouvain.be

Benoit Champagne
UNamur,
Département de Chimie
Rue de Bruxelles, 61
5000 Namur
benoit.champagne@unamur.be

Cédric Malherbe
ULiège,
Département de Chimie
Quartier Agora,
allée du six Août 11
4000 Liège 1
c.malherbe@uliege.be

Infographisme
emmanuel@norproduction.eu**Comité de rédaction**

Kristin Bartik, ULB
Nicolas Blanchard, Université de Haute-Alsace-Université de Strasbourg
Sophie Carenco, Sorbonne Université, Paris
Frédéric Castet, Université de Bordeaux
André Colas, Dow Corning
Damien Debecker, UCLouvain
Karolien De Wael, UAntwerpen
Philippe Dubois, UMons
Anne-Sophie Duwez, ULiège
Gwilherm Evano, ULB
Danielle Fauque, Université de Paris Sud
Stéphane Gérard, Faculté de Pharmacie, Reims
Bernard Joris, ULiège
Sophie Laurent, UMons
Tatjana Parac-Vogt, KU Leuven
Raphaël Robiette, UCLouvain
Cédric Samuel, École des Mines de Douai
Armand Soldera, Université de Sherbrooke
Johan Wouters, UNamur

Secrétariat

Violaine SIZAIRE
ULB
avenue Franklin Roosevelt 50, CP 160/07 1050 Bruxelles
Tel : +32 2 650 52 08 Fax : +32 2 650 51 84 - email : src@ulb.be
Forts : BE60 2100 4208 0470

Comité directeur**Conseil de gestion**

Présidente	A.-S. Duwez, ULiège	asduwez@uliege.be
Vice-président	J.-P. Lecomte, DOW	j.lecomte@dow.com
Président sortant	L. Provin, UCB	laurent.provins@ucb.com
Secrétaire générale	C. Buess-Herman, ULB	Claudine.Buess-Herman@ulb.be
Tresorier	P. Laurent, ULB	Pascal.Laurent@ulb.be
Délégué relations extérieures	P. Baekelmans, Solvay	paul.baekelmans@solvay.com

Divisions

Chimie Médicinale	L. Provin, UCB	laurent.provins@ucb.com
Chimie organique et bio-organique		
Jeunes Chimistes	M. Larry, ULiège	max.larry@uliege.be
Histoire et Enseignement de la Chimie	T. Massenet, ULiège	thibault.massenet@uliege.be
Délégué Essencia Wallonie	B. Van Tiggelen	vantiggelen@memosciences.be
	C. Moucheron, ULB	Cecile.Moucheron@ulb.be
	T. Randoux, Certech	Thierry.Randoux@certech.be

Sections locales

Bruxelles	G. Evano, ULB	Gwilherm.Evano@ulb.be
Louvain-la-Neuve	B. Elias, UCLouvain	benjamin.elias@uclouvain.be
Mons	P. Gerbaux, UMONS	pascal.gerbaux@umons.ac.be
Liège	A. S. Duwez, ULiège	asduwez@ulg.ac.be
Namur	B. Champagne, UNamur	benoit.champagne@unamur.be

Membres protecteurs de la SRC

ALLNEX
CERTECH
EXXONMOBIL CHEMICAL
LHOIST
SOLVAY
TOTALENERGIES
UCB

Parution : trimestrielle

Avec le soutien du Fonds National de la Recherche Scientifique.
Les articles paraissant dans Chimie nouvelle sont repris dans CHEMICAL ABSTRACTS

Editeur responsable : Claudine Buess-Herman,
ULB, CP 160/07,
avenue Roosevelt 50, 1050 Bruxelles

Les articles sont soumis à un processus de reviewing.
Les annonces publicitaires sont établies sous la responsabilité des firmes.

« CHIMIE NOUVELLE » est un titre déposé

ISSN 0771-730X

Alice MATTIUZZI,^a Anne-Marie BAUDUIN,^a Ludovic TROIAN-GAUTIER,^{b,c} Ivan JABIN

^a X4C, Rue Auguste Piccard 48, B-6041 Gosselies, Belgium.

^b Present adress: Institut de la Matière Condensée et des Nanosciences (IMCN),
Molecular Chemistry, Materials and Catalysis (MOST),
Université catholique de Louvain (UCLouvain), Place Louis Pasteur 1, bte L4.01.02,
1348 Louvain-la-Neuve, Belgium.

^c Laboratoire de Chimie Organique, Université libre de Bruxelles (ULB),
avenue F. D. Roosevelt 50, CP160/06, B-1050 Brussels, Belgium.

A.Mattiuzzi is a co-founder and the CEO of X4C. A.-M.Bauduin is in charge of the business development and IP of X4C. L.Troian-Gautier was postdoctoral researcher for X4C in 2014/2015. I.Jabin is a co-founder of X4C and a consultant for X4C.

X4C - Innovative surface functionalization for efficient diagnostic tests

1. Company

X4C SA is a Gosselies-based (Charleroi, Belgium) company that emerged in 2016 as a spin-off from the Université libre de Bruxelles (ULB). X4C was co-founded by Alice Mattiuzzi, CEO, who holds a PhD in chemistry from ULB and Prof. Ivan Jabin, who is the co-director of the Laboratoire de Chimie Organique at ULB. Through the development of calix[4]arene-based advanced coatings, X4C aims to provide robust solutions for providing *à la carte* surface properties and functionalities to materials for high-end applications. A major priority of X4C is to grow on the market of *in vitro* diagnostic tests (IVD) by improving the overall sensitivity, specificity and cost-effectiveness of IVD diagnostic kits. To reach these goals, X4C develops and licenses tailored coating solutions to answer not only specific needs of companies that develop IVD tests, but also those that supply reagents such as functionalized nanoparticles (NPs) and surfaces as essential components of high-performance IVD tests.

2. History and main activities

X4C's technology is based on scientific discoveries made by Alice Mattiuzzi, Ivan Jabin and French

colleagues (Profs Corinne Lagrost and Olivia Reinaud) in the field of surface functionalization. They showed that calix[4]arene-diazonium salts (Figure 1) can be used as molecular platforms for the modification of surfaces (of any nature, shape and dimension) through the formation of ultra-stable, post-functionalizable and covalently grafted monolayers. From 2016 to 2020, X4C focused on developing industrial partnerships that could *a priori* benefit from monolayers of calix[4] arene coatings for improving or creating new surface properties or functionalities. Companies in both non-medical sectors (electronics and opto-electronics, surface treatment etc.) and the medical sector (medical devices and IVD) have been approached and their yet unmet needs have been collected. In the non-medical sectors, improvement avenues encompassed self-cleaning, anti-biofouling, anti-frosting, anti-fogging, and water-proofing. In the medical sector, the main unmet needs have emerged from companies developing implantable medical devices, where a strong desire to improve bio-/hemocompatibility and surface lubrication of stents was expressed, as well as from companies developing IVD tests that seek to improve their sensitivity and specificity. Nowadays, X4C focuses on further reducing the "gap" between their technology implementation and the unmet needs of main

players. To bridge that gap, X4C develops proofs of concept (PoCs) for evidencing the advantages of X4C technology compared to other existing methods for surface functionalization. This approach has enabled X4C to identify the medical sector as the most promising one, because of the necessity for high-end surface functionalization where classical surface treatments often fail or generate unsatisfactory results. X4C has carried out several technical feasibility studies to measure the suitability of its technology. These have allowed to i) better show the basic strengths of the calix[4]arene coating technology, ii) document the unmet expectations of stakeholders in the fields of *in vitro* diagnostics and implantable medical devices (stents) and iii) collect preliminary data on X4C differentiation factors compared to other coatings available on the market. Since mid-2020, X4C has decided to focus solely on medical applications and especially on the improvement of IVD diagnostic kits in view of leading to commercial deals.

3. IVD field

Today, the vast majority of *in vitro* diagnostic tests are based on the biorecognition between an analyte (e.g. an antigen) present in a matrix (physiological fluid, possibly pretreated) and a receptor (e.g. an antibody) located at the surface of a transducer that converts the information related to biorecognition into a measurable signal (e.g. an optical signal). Transducers can have different shapes and dimensions (a flat surface in the case of biosensors, a microparticle or a nanoparticle used as colorimetric reporters in the case of lateral flow immunoassays (LFAs)). The intensity of the signal depends on the characteristics and intrinsic properties of the transducer (e.g. nature, shape, size and optical properties of (nano)particle-based colorimetric reporters such as gold nanoparticles, silver nanoparticles or latex beads) as well as on the quality of the biorecognition (e.g. antibody-antigen) in terms of specificity, reproducibility and accuracy.

Currently, companies who are active in the development of immunoassays (antibody-antigen recognition) *in vitro* diagnostic devices are seeking

to improve detection sensitivity and specificity, thereby improving their bioanalytical method. To this end, they aim to achieve the ideal combination of the most appropriate transducers on the surface of which the receptor (e.g. antibody) is grafted in an optimal arrangement in terms of packing and orientation for effective recognition. The main challenges associated with such optimized arrangement include: (a) developing a robust grafting methodology to immobilize the receptor (e.g. antibody) and ensure high stability of resulting bioconjugate (stability over long periods of time and stability in the experimental conditions of the test and storage); (b) controlling the grafting density and its regularity for yielding a homogeneous distribution of the receptor (e.g. antibody) all over the surface; (c) controlling the orientation of the antibody during its immobilization to optimize the antibody-antigen recognition process; (d) limiting non-specific responses.

Polystyrene microbeads and gold nanoparticles (AuNPs) are widely used in immunoassay diagnostic devices (bead-based ELISA, immunoturbidity, lateral flow, etc.). Most frequently, receptors are immobilized by passive adsorption, which often leads to considerable desorption or denaturation in the case of antibodies or other proteins. Other strategies, such as the covalent bioconjugation by peptide type coupling between -COOH groups located at the surface of the polystyrene microbeads or gold nanoparticles and -NH₂ groups of the receptor have been developed. However, relying on the currently available COOH-functionalized AuNPs and polystyrene beads, neither passive adsorption nor peptide type coupling-based covalent bioconjugation offer a means to control the number of immobilized antibodies and/or their orientation.

4. X4C core Technology

In the field of *in vitro* diagnostic devices, X4C's technology offers different key differentiating advantages for coating the surface of a broad scope of frequently used transducers (Figure 1). X4C's core technology consists of the covalent and controlled grafting of a robust and compact organic monolayer of calix[4]arenes either on conductive

(gold, silver, carbon, steel, etc.) or semi-conductive (e.g. germanium) surfaces as well as on insulators (e.g. glass) and polymeric materials (PS, PE, etc.) [1]. Besides, these surfaces can be of any shape or dimension (flat surface, micro- or nanoparticle, large or small). Calix[4]arene-tetradiazonium salts present four anchoring points and can thus potentially form up to four chemical bonds with the surface (each aryl diazonium group can generate an highly reactive aryl radical in reductive conditions). This leads to a remarkable stability of the calixarene-based coating that outperforms that of other classical organic coatings (SAMs of thiols, classical aryl diazoniums, etc.). The monolayer of calix[4]arenes is also bearing additional reactive groups ($R = \text{carboxyl, alkyne, etc.}$) that enables post-functionalization with specific molecules or biomolecules (antibodies, peptides, DNA, etc.). Hence, this approach is highly customizable and can be rapidly adapted to meet the customers' needs.

Since a few years, X4C has developed a strong collaboration with the groups of Gilles Bruylants and Ivan Jabin (both at ULB) aiming at developing new calixarene-coated nanomaterials and their use as enhanced colorimetric reporters for IVD applications (patent application filed). In this context, X4C has been granted an exclusive license to use a straightforward one-pot method of preparation of metal nanoparticles (gold, silver, etc.) coated with functionalizable calix[4]arenes (Figure 1). The robustness of the monolayer of calix[4]arenes is a striking feature of the resulting calix[4]arene-coated nanomaterials. Indeed, classical gold nanoparticles (AuNPs) capped by citrate anions readily degrade or aggregate with changes in pH, ionic strength, or in the presence of large concentration of fluoride. In contrast, calixarene-capped AuNPs (calix-AuNPs) remain stable upon extreme pH variation, in the presence of large concentrations of fluoride ions (between 0.15 and 0.75 M) or under increased ionic strength

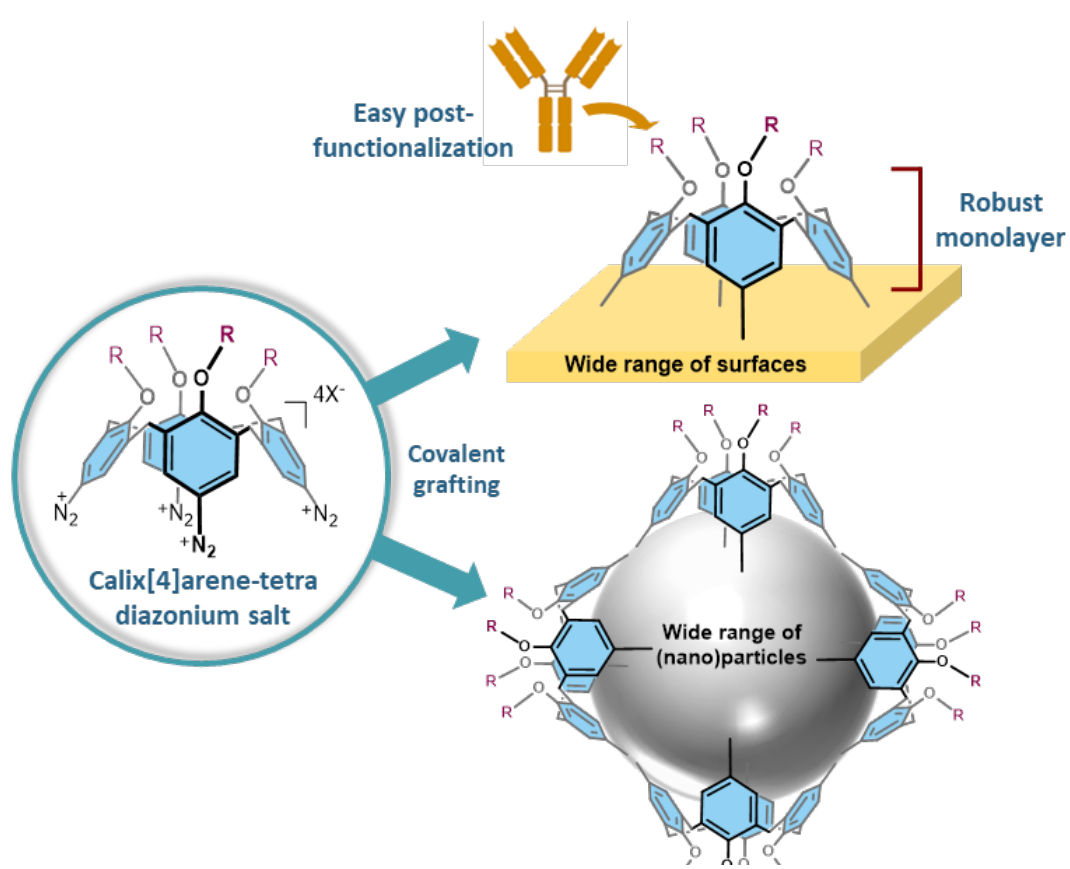


Figure 1: Core technology of X4C.

(Figure 2a) [2]. Even more remarkably, calix-AuNPs can be completely dried, yielding a gold-colored film, and then resuspended, without any loss in their optical properties (Figure 2b).

X4C technology shows its full effect especially for the preparation of particles known to be unstable so far. This is the case of silver nanoparticles (AgNPs). The latter are particularly attractive as colorimetric reporter candidates in IVD tests such as LFIAs because their intrinsic optical properties are better compared to AuNPs and they are significantly cheaper than AuNPs [3]. However, AgNPs are currently not commercially used for *in vitro* diagnostic tests because of major concerns regarding their stability. Functionalizing their surface remains thus an obstacle, limiting the bioconjugation possibilities [4]. This stability problem has been solved by using X4C's technology. Ultra-stable calixarene-capped silver nanoparticles (AgNPs-calix) have been successfully prepared. They do not aggregate even after drying (70°C) and withstand severe etching conditions [5]. Moreover, calixarene-capping prevents aggregation and degradation during and after bioconjugation (covalent and adsorption) to proteins without any loss of stability observed after at least 6 months (Figure 2c).

In addition to provide extremely robust monolayers, X4C's technology is also used to efficiently control the grafting density of specific functions. For example, a mixture of calix[4] arenes, each bearing different functional groups, e.g. oligo(ethylene glycol) chains and carboxyl groups, leads to the formation of a monolayer whose composition reflects the ratio of calix[4] arenes used in the grafting solution [6]. To our knowledge, this is a unique and simple approach to control the 2D surface structuring, grafting density and thus bioconjugation.

5. Applications in IVD field

The use of calix[4]arene tetradiazonium derivatives has already found applications in biosensing, lateral flow immunoassays (LFIAs) and immunoturbidimetry [7]. Two recent examples are described hereinafter.

Germanium-based biosensors for proteins [8]. Fourier transform infrared (FTIR) spectroscopy is a promising technique for the detection of proteins in complex media [9]. Classical FTIR-based biosensors require an organic layer functionalized with a biological receptor, which is directly grafted onto the internal reflection

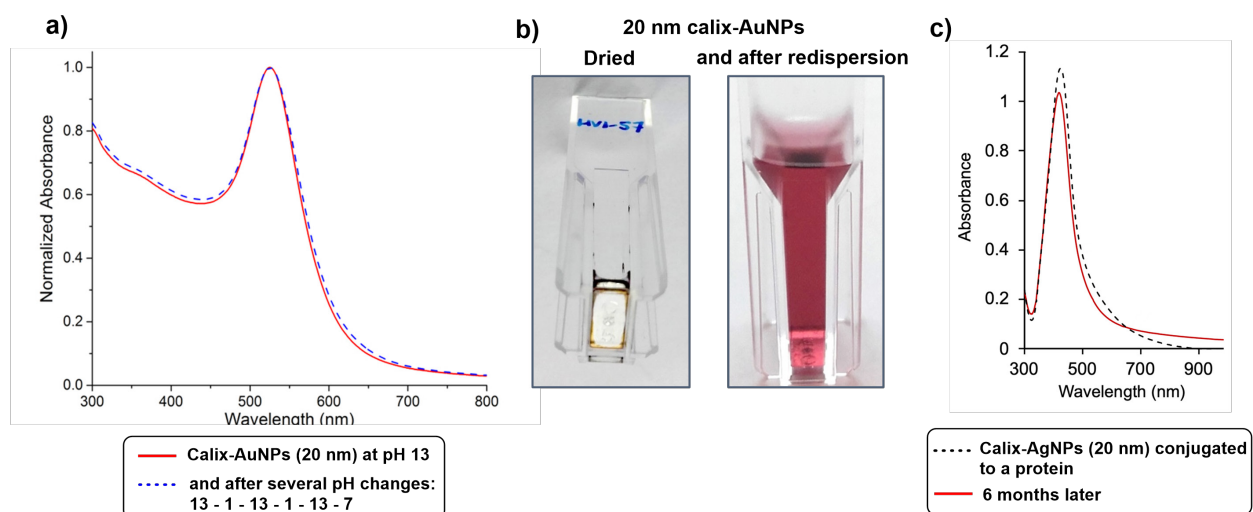


Figure 2: a) UV-Vis spectra of 20 nm calix-AuNPs at pH 13 (red solid line) and after several pH changes (blue dashed line); b) Pictures of dried 20 nm calix-AuNPs (left) and after redispersion in water (right); c) UV-Vis spectra of calix-AgNPs conjugated to a protein (black dashed line) and 6 months later (red solid line).

element [10]. However, the grafting of stable and thin organic layers on germanium surfaces remains a topical challenge [9^a, 11]. X4C's technology was able to break technological barriers through the robust anchoring of a calix[4]arene derivative decorated with three oligo(ethylene glycol) (oEG) chains terminated by a methoxy group and one oEG chain terminated by a carboxyl group (Figure 3 left). The grafted calixarene monolayer prevents non-specific adsorption of proteins through the oEG chains while the carboxyl group allows bioconjugation with biomolecules such as bovine serum albumin or biotin. The resulting calix[4]arene-biotin-based germanium biosensors were then used to selectively detect streptavidin (SA) from a complex medium by a combination of ATR-FTIR spectroscopy and fluorescence microscopy. The IR spectra show the characteristic amide-I and amide-II IR absorption bands at 1637 cm⁻¹ and 1535 cm⁻¹, respectively (Figure 3a), which confirms the recognition of streptavidin (100mg/mL). Recognition was also effective with streptavidin in the presence of bovine serum albumin (BSA) (100 µg/mL). Very interestingly, no contribution from BSA at 1657 cm⁻¹ can be detected in the spectra obtained from incubation experiments

in the presence of this protein, which highlights the remarkable antifouling properties of the calixarene-coated germanium surfaces. Similar strategies were also developed using fluorescent FITC-BSA (100 µg/mL) and streptavidin-ATTO655 (100 µg/mL), for which the specific interaction with biotin-spotted germanium surface generated a fluorescent microarray corresponding to the immobilized biotin pattern (Figure 3b).

Use of AgNPs-calix for the serological detection of Anti-SARS-CoV-2 IgG in human samples [12]. Among all of the rapid diagnostic tests developed over the past years, LFIAs are probably the most widely used [13]. Indeed, LFIAs combine all of the POC (Point-Of-Care) features such as simple read-out signal, low cost and ease of use [14]. AuNPs are classically used as the colorimetric reporter in LFIAs because these plasmonic nanomaterials exhibit interesting optical properties [15]. Nevertheless, if compared to ELISAs current AuNPs-based LFIAs suffer from a poor sensitivity. One approach for improving the sensitivity of LFIAs is to use a colorimetric reporter exhibiting better optical properties than AuNPs, such as AgNPs [3]. Provided AgNP-based bioconjugates are stable, corresponding AgNP-based LFIAs

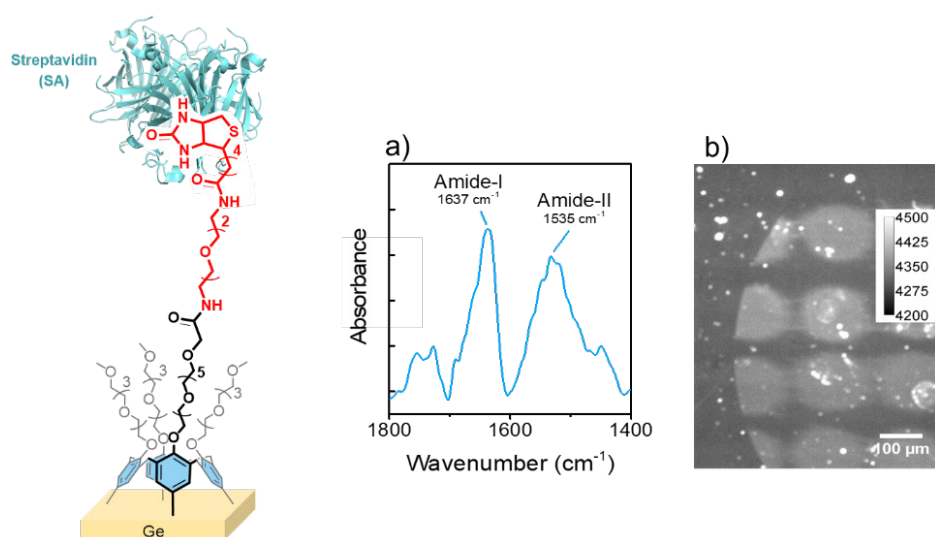


Figure 3: Left: FTIR-based selective biosensor for streptavidin (SA) composed of a calix[4]arene-biotin based germanium surface. Right: a) ATR-FTIR absorption spectra obtained after incubation in a solution of SA; b) fluorescence image acquired on Ge-calix[4]arene-biotin-spotted surface that was incubated with fluorescent streptavidin-ATTO655.

are expected to offer serological tests with lower detection limits compared to AuNP-based LFIA. The use of AgNPs has, however been scarcely reported for the detection of proteins due to the weak chemical and colloidal stability of AgNPs in general and in complex media in particular. Here again, X4C's technology led to very promising results, paving the way to a commercial use of silver nanomaterials in the IVD field. The covalent bioconjugation of the receptor binding domain of the SARS-CoV-2 Spike Protein (Prot-S) was performed on calix[4]arene-functionalized AgNPs. The calixarene coating conferred remarkable stability to the resulting bioconjugated AgNPs in complex media such as human plasma, as no degradation was observed over several months. Simplified LFIA tests (dipstick experiments) using the resulting bioconjugated AgNPs were developed and used for the detection of Anti-SARS-CoV-2 IgG in clinical samples (Figure 4).

In comparison with LFIA based on classical gold nanoparticles, calixarene-based AgNPs significantly improved the limit of detection (LOD) for Anti-SARS-CoV-2 IgG since the LOD was reduced by one order of magnitude and similar signals were observed with 10 times fewer particles. In real clinical samples of patient who tested positive (RT-PCR) for SARS-CoV-2

infection, the AgNP-based dipstick assays showed impressive results: 100% specificity was observed for negative samples, while a sensitivity of 73% was determined for positive samples (Figure 5).

6. Conclusion

The use of calix[4]arene-diazonium salts for the modification of surfaces enables the formation of robust, dense and post-functionalizable monolayers on a great variety of materials, in particular, those that are frequently used in the field of IVD such as (nano)particles. In addition, monolayers of controlled composition of different calix[4]arenes can be readily obtained when a mixture of them is used during the grafting process, which offers an elegant approach to fine-tune the subsequent organization of receptors at the surface of such materials. One of the most spectacular achievement is the formation of ultra-stable nanomaterials such as calixarene-coated gold or silver nanoparticles. X4C has developed several demonstrators to show corresponding key advantages. Alongside, X4C has improved its knowledge of the IVD market and has initiated several co-developments with industrial partners in this field in view of leading to commercial deals. X4C is continuously balancing its efforts between,

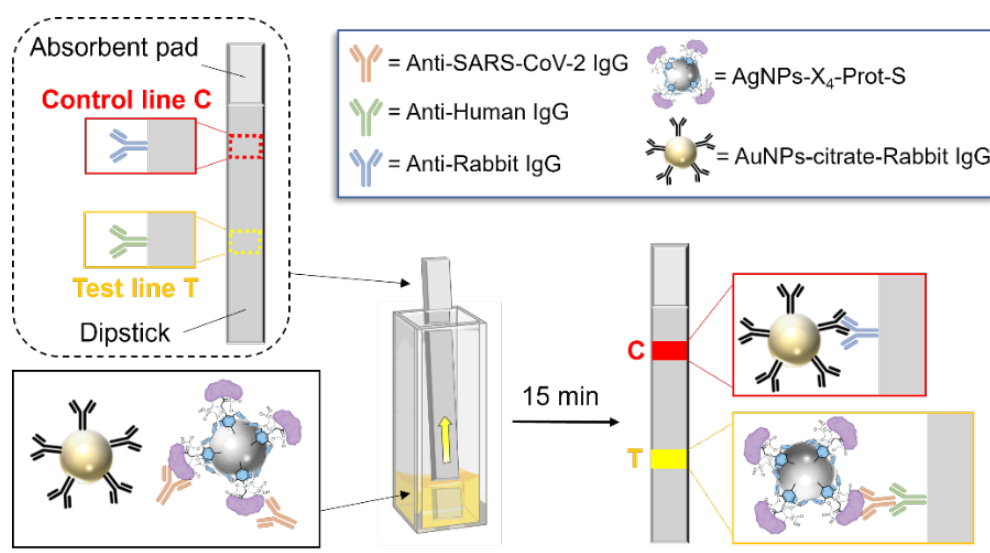


Figure 4: Dipstick assay principle for the detection of Anti-SARS-CoV-2 IgG with calixarene-coated AgNPs.

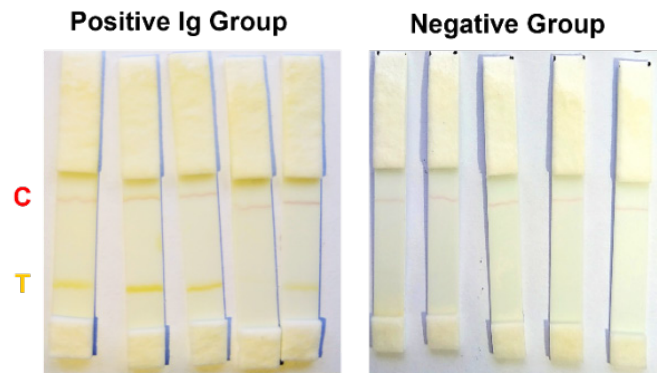


Figure 5: Pictures of dipstick assays for the serological detection of Anti-SARS-CoV-2 IgG in real human samples.
Left) Example of positive sample group; Right) negative samples.

on the one hand, solving client's issues related to IVD tests performance linked to the transducer surface properties and functionalities and, on the other hand, expanding its own portfolio of calix[4] arene-coated materials including next generation particles in the field of IVD.

Acknowledgements

The authors thank Sara Wehlin for assistance in proofreading.

References

- [1] (a) Mattiuzzi, A.; Jabin, I.; Mangeney, C.; Roux, C.; Reinaud, O.; Santos, L.; Bergamini, J.F.; Hapiot, P.; Lagrost, C. *Nat. Commun.* **2012**, *3*, 1130. (b) Troian-Gautier, L.; Martinez-Tong, D.; Hubert, J.; Reniers, F.; Sferrazza, M.; Mattiuzzi, A.; Lagrost, C.; Jabin, I. *J. Phys. Chem. C* **2016**, *120*, 22936-22945. (c) Troian-Gautier, L.; Mattiuzzi, A.; Reinaud, O.; Lagrost, C.; Jabin, I. *Org. Biomol. Chem.* **2020**, *18*, 3624-3637. (d) Troian-Gautier, L.; Mattiuzzi, A.; Blond, P.; Retout, M.; Bruylants, G.; Reinaud, O.; Lagrost, C.; Jabin, I. in *Aryl Diazonium Salts and Related Compounds. Surface Chemistry and Applications*, Pinson J.; Mousli, F. Chehimi M. M. Eds, Springer, 2022, Chapter 13, pp 247-262.
- [2] Troian-Gautier, L.; Valkenier, H.; Mattiuzzi, A.; Jabin, I.; Van den Brande, N.; Van Mele, B.; Hubert, J.; Reniers, F.; Bruylants, G.; Lagrost, C.; Leroux, Y. *Chem. Commun.* **2016**, *52*, 10493-10496.
- [3] Lee, J.-S.; Lytton-Jean, A. K. R.; Hurst, S. J.; Mirkin, C. A. *Nano Lett.* **2007**, *7*, 2112-2115.
- [4] Pinzaru, I.; Coricovac, D.; Dehelean, C.; Moaca , E.-A.; Mioc, M.; Baderca, F.; Sizemore, I.; Brittle, S.; Marti, D.; Calina, C. D.; Tsatsakis, A. M.; Soica, C. *Food Chem. Toxicol.* **2018**, *111*, 546-556.
- [5] Retout, M.; Jabin, I.; Bruylants, G. *ACS Omega* **2021**, *6*, 19675-19684.
- [6] (a) Santos, L.; Mattiuzzi, A.; Jabin, I.; Vandencasteele, N.; Reniers, F.; Reinaud, O.; Hapiot, P.; Lhenry, S.; Leroux, Y.; Lagrost, C. *J. Phys. Chem. C* **2014**, *118*, 15919-15928 (b) Valkenier, H.; Malytskyi, V.; Blond, P.; Retout, M.; Mattiuzzi, A.; Goole, J.; Raussens, V.; Jabin, I.; Bruylants, G. *Langmuir* **2017**, *33*, 8253-8259.
- [7] (a) Retout, M.; Blond, P.; Jabin, I.; Bruylants, G. *Bioconjugate Chem.* **2021**, *32*, 290-300. (b) Retout, R.; Gosselin, B.; Mattiuzzi, A.; Ternad, I.; Jabin, I.; Bruylants, G. *ChemPlusChem* **2022**, *87*, e202100450.
- [8] Blond, B.; Bevernaegie, R.; Troian-Gautier, L.; Lagrost, C.; Hubert, J.; Reniers, F.; Raussens, V.; Jabin, I. *Langmuir* **2020**, *36*, 12068-12076.
- [9] (a) de Jongh, H. H. J.; Goormaghtigh, E.; Ruysschaert, J.-M. *Biochemistry* **1997**, *36*, 13603–13610. (b) Goormaghtigh, E.; Gasper, R.; Bénard, A.; Goldsztein, A.; Raussens, V. *Biochim. Biophys. Acta, Proteins Proteomics* **2009**, *1794*, 1332–1343.
- [10] (a) Goldzstein, A.; Aamouche, A.; Homble , F.; Voue, M.; Conti, J.; De Coninck, J.; Devouge, S.; Marchand-Brynaert, J.; Goormaghtigh, E. *Biosens. Bioelectron.* **2009**, *24*, 1831–1836. (b) Schartner, J.; Guldenhaupt, J.; Katharina, G.; Rosga, K.; Kourist, R.; Gerwert, K.; Kotting, C. *Analyst* **2018**, *143*, 2276–2284.
- [11] (a) Schartner, J.; Gavriljuk, K.; Nabers, A.; Weide, P.; Muhler, M.; Gerwert, K.; Kotting, C. *ChemBioChem* **2014**, *15*, 2529–2534. (b) Girard, A.; Geneste, F.; Coulon, N.; Cardinaud, C.; Mohammed-Brahim, T. *Appl. Surf. Sci.* **2013**, *282*, 146–155.
- [12] Gosselin, B.; Retout, M.; Dutour, R.; Troian-Gautier, L.; Bevernaegie, R.; Herens, S.; Lefèvre, P.; Denis, O.; Bruylants G.; Jabin, I. *Anal. Chem.* **2022**, *94*, 7383-7390.
- [13] Huang, C.; Wen, T.; Shi, F.-J.; Zeng, X.-Y.; Jiao, Y.-J. *ACS Omega* **2020**, *5*, 12550–12556.
- [14] Soh, J. H.; Chan, H.-M.; Ying, J. Y. *Nano Today* **2020**, *30*, 100831.
- [15] Liu, X.; Atwater, M.; Wang, J.; Huo, Q. *Colloids Surf. B* **2007**, *58*, 3–7.



Cédric THEUNISSEN

Laboratoire de Chimie Organique,
Service de Chimie et PhysicoChimie Organiques,
Université libre de Bruxelles ULB,
Avenue F. D. Roosevelt 50, CP160/06,
B-1050 Bruxelles, Belgique.
Cedric.Theunissen@ulb.be

Activation de Liaisons Carbone – Azote et Utilisation des Sels d'Ammonium comme Précureurs de Radicaux

Résumé

L'activation de liaisons généralement considérées comme inertes telles que les liaisons C-N revêt une importance fondamentale pour le développement de nouveaux procédés de synthèse innovants, efficaces et plus respectueux de l'environnement. Malgré des progrès récents, la génération de radicaux par activation de liaisons C-N souffre encore de limitations liées à l'utilisation de précurseurs de radicaux loin d'être idéaux. Dans ce contexte, les sels d'ammonium constituent une alternative de choix et un intérêt grandissant pour leur activation s'est manifesté au cours des dernières années. Cet article décrit nos travaux récents concernant l'activation de sels d'ammonium par catalyse photorédox à l'iridium et l'exploitation des radicaux ainsi formés pour le développement de réactions d'hydrodéamination et de couplages radicalaires. Finalement, la voltammetrie cyclique a été exploitée pour rationaliser les profils de réactivité observés expérimentalement.

Carbon – Nitrogen Bond Activation and Use of Ammonium Salts as Convenient Radical Precursors

Abstract

The activation of inert bonds such as C–N bonds is of prime importance for the development of new, innovative and eco-friendly chemical processes. Despite recent progress, the generation of radicals by C–N bond activation still suffers

from the use of radical precursors far from being ideal. In this context, ammonium salts constitute an attractive alternative and a growing interest has been devoted to their activation in the past few years. This article describes our recent work on the activation of ammonium salts using iridium photoredox catalysis and the use of the corresponding radicals for the development of hydrodeamination reactions and radical couplings. Finally, cyclic voltammetry was exploited to rationalize the reactivity profile observed experimentally.

Keywords

*C–N bond activation ; Radical chemistry ;
Ammonium salts ; Photoredox catalysis*

1. Introduction générale : importance de l'activation de liaisons carbone – azote

L'importance fondamentale de la synthèse organique dans notre vie quotidienne et dans différents domaines tels que la chimie médicinale, la biologie, les polymères ou encore en science des matériaux est indéniable. Il en résulte une demande toujours plus forte pour la mise au point de nouvelles méthodes de synthèse permettant la préparation de molécules organiques complexes ou biologiquement actives. Ces méthodes doivent être toujours plus efficaces, rapides et respectueuses de l'environnement afin de réduire l'empreinte environnementale de la chimie de synthèse sur l'environnement. Au vu de la crise

énergétique actuelle, il est également impératif de s'affranchir de l'utilisation de matières premières issues du pétrole qui restent encore surexploitées dans l'industrie chimique de nos jours. Ces exigences requièrent le développement de nouvelles stratégies pour assembler rapidement des molécules organiques complexes au départ de réactifs simples, peu coûteux et renouvelables. Dans cette optique, l'activation de liaisons traditionnellement considérées comme inertes revêt une importance cruciale puisqu'elle ouvre de nouvelles perspectives en synthèse organique moderne pour l'élaboration de voies de synthèse innovantes et reposant sur l'utilisation de matières premières bio-sourcées. Si l'activation de liaisons carbone – hydrogène a profondément impacté la synthèse organique, celle de liaisons carbone – azote est restée sous exploitée pendant longtemps, probablement à cause de leur énergie de dissociation élevée qui les rend très stables et donc peu réactives. Néanmoins, l'activation de liaisons C-N présente un énorme potentiel pour le développement de procédés plus respectueux de l'environnement puisque les amines, et nombre de leurs dérivés, sont maintenant facilement obtenues au départ de la biomasse, grâce notamment à la valorisation de la lignine et de la chitine [1]. Le développement de nouveaux procédés innovants reposant sur l'activation de liaisons C-N au départ de matières premières renouvelables, simples et peu coûteuses aura très certainement un impact majeur sur la chimie de synthèse et dans de nombreux autres domaines dans les années à venir.

2. Activation radicalaire de liaisons carbone – azote

2.1. Principaux précurseurs de radicaux dérivés d'amines

Au cours de la dernière décennie, un intérêt grandissant s'est manifesté pour l'activation de liaisons carbone – azote mais les procédés faisant intervenir la génération et l'exploitation d'espèces radicalaires sont restés sous-exploités malgré un potentiel évident [2-4]. En effet, la chimie radicalaire est connue depuis des décennies pour promouvoir une variété de

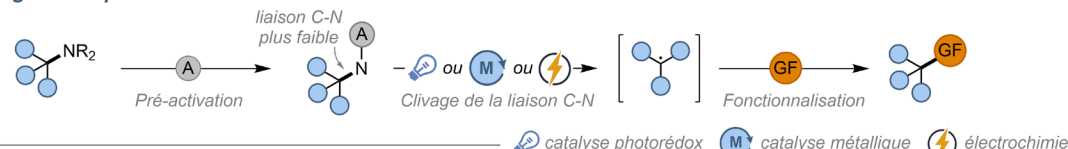
transformations avec des niveaux d'efficacité et de sélectivité particulièrement élevés [5]. Son utilisation est cependant restée limitée pendant longtemps par la nécessité d'utiliser des dérivés de l'étain ou des peroxydes, particulièrement toxiques et dangereux, qui ont drastiquement restreint son intérêt synthétique. Plusieurs stratégies, telles que la catalyse photorédox [6-7], la catalyse à l'aide de métaux de transition [8] et l'électrochimie [9-10], ont récemment été développées pour faciliter la génération et mieux contrôler la réactivité des radicaux en conditions douces, permettant ainsi de pallier cette limitation majeure.

La génération de radicaux par activation de liaisons carbone – azote nécessite généralement de pré-activer les amines de départ afin de générer des précurseurs de radicaux plus réactifs. A l'heure actuelle, les principaux précurseurs de radicaux dérivés d'amines sont les sels de diazonium [11-12], les sels de Katritzky [13] ainsi que, dans une moindre mesure, les imines rédox-actives [14-15] (Figure 1). Ces dérivés ont en effet déjà prouvé leur efficacité dans une série de transformations radicalaires donnant accès à différentes molécules d'importance en synthèse organique moderne, et trois exemples représentatifs sont brièvement présentés à la Figure 1. Les sels de diazonium ont notamment été activés par catalyse photorédox et couplés à des hétérocycles riches en électrons pour la synthèse de biaryles, qui sont des motifs d'une grande importance en synthèse organique et en chimie médicinale [16]. Plus récemment, l'utilisation de la catalyse au nickel a été mise à profit pour générer des radicaux au départ de divers sels de Katritzky et promouvoir des réactions de couplages croisés avec des acides boroniques en conditions douces [17]. Finalement, l'activation d'imines rédox-actives par catalyse photorédox a également été exploitée pour le développement de nouvelles réactions de Giese offrant un accès rapide et efficace à divers composés possédant un atome de carbone quaternaire [14]. Malgré un intérêt évident, ces composés souffrent néanmoins de diverses limitations qui impactent sévèrement leur utilité synthétique. Les sels de diazonium permettent en effet de générer des radicaux aryles avec une excellente économie

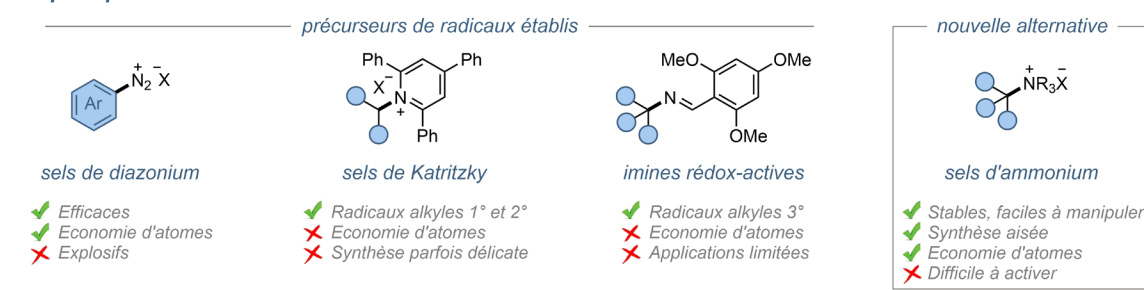
d'atomes (diazote libéré comme sous-produit de la réaction) mais leur utilisation pose problème en terme de sécurité de par leur caractère explosif. Les sels de Katritzky et les imines rédox-actives permettent quant à eux de générer des radicaux alkyles en conditions douces mais avec une très mauvaise économie d'atomes. L'activation et le clivage des liaisons C-N d'intérêt de ces précurseurs s'accompagnent en effet de la génération de sous-produits particulièrement volumineux (la 2,4,6-triphénylpyridine et le 2,4,6-triméthoxybenzonitrile) qui sont très souvent plus lourds que les radicaux alkyles d'intérêt. Afin de pallier ces limitations, il est donc nécessaire de développer de nouveaux procédés

reposant sur l'activation de liaisons C-N au départ de précurseurs de radicaux plus attrayants. Dans cette optique, les sels d'ammonium constituent une alternative particulièrement intéressante puisqu'ils sont stables, non-toxiques, sûrs d'utilisation et facilement synthétisables à grande échelle [18]. Ils sont également particulièrement attractifs en termes d'économie d'atomes puisque le clivage de leur liaison C-N s'accompagne de la génération d'une simple trialkylamine comme seul sous-produit de la réaction. En conséquence, un intérêt marqué s'est manifesté au cours des dernières années pour le développement de nouveaux procédés de synthèse au départ de sels d'ammonium [19].

Stratégie générale pour l'activation radicalaire de liaisons C-N

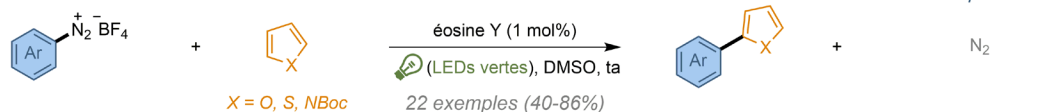


Principaux précurseurs de radicaux

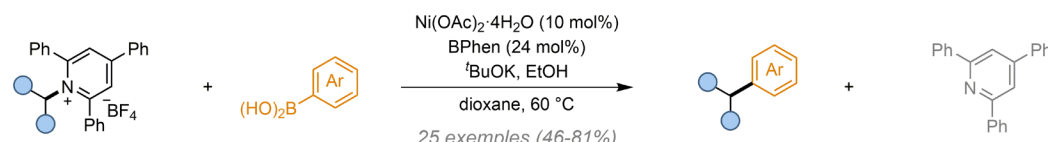


Transformations représentatives

Synthèse de biaryles au départ de sels de diazonium



Couplages croisés au départ de sels de Katritzky



Réactions de Giese au départ d'imines rédox-actives

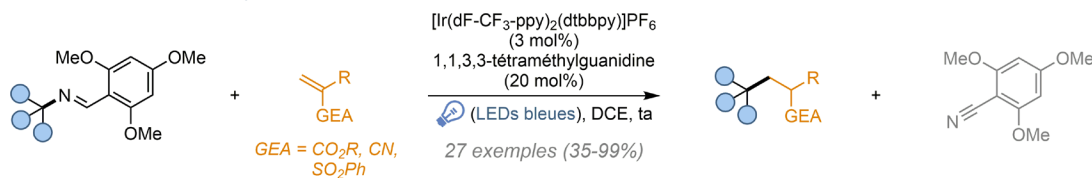


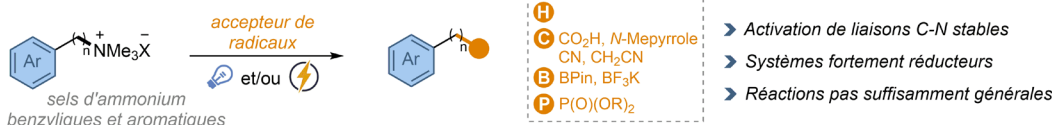
Figure 1. Activation radicalaire de liaisons C-N : stratégie générale, principaux précurseurs de radicaux et transformations représentatives.

2.2. Activation radicalaire de sels d'ammonium : état de l'art

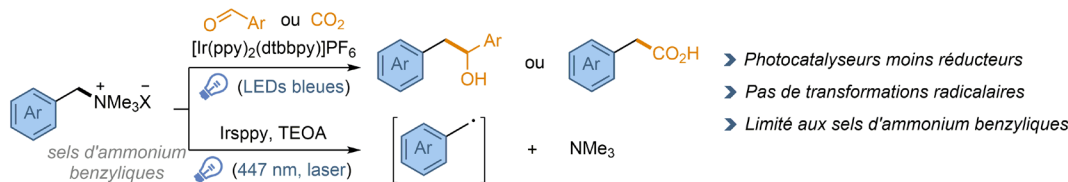
Si la plupart des procédés de déamination développés au départ des sels d'ammonium reposent sur une activation par addition oxydante sur un catalyseur métallique, leur activation radicalaire est longtemps restée peu décrite à cause de la difficulté associée à leur réduction. Au cours des dernières années, plusieurs procédés de déamination radicalaires élégants ont été décrits au départ de sels d'ammonium, certains reposant notamment sur l'utilisation de la catalyse photorédox et de l'électrochimie. Certains sels d'ammonium benzyliques et aromatiques ont ainsi pu être engagés dans des réactions de réduction [20-23], de carboxylation [24-25], d'amino/alcooxycarbonylation [26], de borylation [27-31], de phosphorylation [32] et de cyanation/cyanométhylation [33] radicalaires (Figure 2). Ces procédés efficaces restent néanmoins limités en termes de praticité et de champs d'application, ne donnant en effet accès qu'à un panel relativement restreint de composés. De plus, la plupart des systèmes décrits sont particulièrement réducteurs, ce qui peut poser des problèmes en termes de compatibilité vis-à-vis de certains groupements fonctionnels sensibles

à la réduction. Dans ce contexte, l'utilisation de la catalyse photorédox reposant sur l'emploi de complexes d'iridium pour l'activation de sels d'ammonium benzyliques constitue une perspective attrayante. En revanche, celle-ci est restée limitée à la double réduction de sels d'ammonium benzyliques puis addition des carbanions benzyliques correspondants sur des dérivés de benzaldéhydes et du dioxyde de carbone [34], ainsi qu'à la dégradation du chlorure de benzyltriméthylammonium à l'aide d'un laser et *via* un mécanisme à deux photons [35-36]. Bien qu'élégants, ces travaux n'exploitent donc pas pleinement le potentiel synthétique des sels d'ammonium en tant que précurseurs de radicaux. Par conséquent, nous nous sommes intéressés à étendre l'utilisation de la photocatalyse à l'iridium afin 1) d'activer des sels d'ammonium aromatiques mais également 2) d'engager ces sels d'ammonium benzyliques et aromatiques dans des réactions d'hydrodéamination et dans des couplages radicalaires. Nous nous sommes concentrés sur l'utilisation de complexes d'iridium comme photocatalyseurs qui prédomine à l'heure actuelle par rapport à celle de complexes de ruthénium et de cuivre. En effet, les complexes d'iridium sont caractérisés par une forte absorption dans

Sels d'ammonium en tant que précurseurs de radicaux



Activation de sels d'ammonium par catalyse photorédox à l'iridium (précédents)



Fonctionnalisation radicalaire par catalyse photorédox à l'iridium (notre travail)



Figure 2. Activation radicalaire de sels d'ammonium : état de l'art et fonctionnalisation radicalaire par photocatalyse à l'iridium.

le domaine du visible, une luminescence intense et de longs temps de vie à l'état excité (de l'ordre de plusieurs centaines de nanosecondes à quelques microsecondes), tandis que leur grande modularité permet en outre d'accéder à une large gamme de potentiels d'oxydation et de réduction. Les principaux résultats obtenus au cours de ces travaux sont décrits dans les paragraphes suivants.

3. Utilisation des sels d'ammonium comme précurseurs de radicaux par catalyse photorédox à l'iridium

3.1. Hydrodéamination de sels d'ammonium benzyliques et aromatiques

Nous avons débuté notre étude par la mise au point d'une réaction d'hydrodéamination de sels d'ammonium benzyliques pour laquelle le système optimal repose sur l'utilisation de $[\text{Ir}(\text{ppy})_2(\text{dtbbpy})]\text{PF}_6$ comme photocatalyseur et d'un excès de la base de Hünig ($(i\text{Pr})_2\text{NEt}$) comme réducteur sacrificiel dans de l'acetonitrile à température ambiante (ta) et sous irradiation avec de la lumière bleue. Dans ces conditions, le champ d'application de la réaction a pu être évalué et divers sels d'ammonium benzyliques ont pu être aisément réduits (Schéma 1). Outre la réduction du sel d'ammonium **1a** utilisé comme substrat modèle lors de l'étape d'optimisation (83%), d'autres groupements aromatiques sont également tolérés, comme illustré par la réduction des sels d'ammonium **1b-d** avec de bons rendements (63-74%). La présence de substituants électroattracteurs tels qu'un cyano **3f**, un ester méthylique **3g** ou un groupement trifluorométhyle **3h** est également bien tolérée (54-95%) tandis que celle de substituants électrodonneurs tels qu'un 3-OBn **3i** ou un 4-Me **3j** inhibe totalement la réaction. Contre toute attente, une absence de réactivité similaire a également été observée au départ du sel d'ammonium benzylique non substitué **1k**. En revanche, la substitution de la position benzylique avec des groupements variés (méthyle, phényle, ester éthylique) est bien tolérée, comme le montre la réduction des sels d'ammonium **1l-n** (60-86%). Finalement,

l'activation de sels d'ammonium dérivés de la pyrrolidine **5** (62%) et du DABCO **6** (77%) a également pu être démontrée.

Par la suite, nous nous sommes intéressés à l'activation plus délicate de sels d'ammonium aromatiques. Celle-ci a nécessité une ré-optimisation des conditions réactionnelles qui reposent maintenant sur l'utilisation d'un photocatalyseur plus réducteur ($\text{Ir}(\text{ppy})_3$) et d'un mélange de base de Hünig et d'acide formique comme réducteur sacrificiel, toujours dans de l'acetonitrile à température ambiante et sous irradiation avec de la lumière bleue. Dans ces conditions, une variété de sels d'ammonium aromatiques a pu être activée et un profil de réactivité similaire à celui de leurs congénères benzyliques a été observé (Schéma 1). Plusieurs sels d'ammonium biarylques ont pu être aisément réduits pour fournir les produits de réduction correspondants **4a-d** avec des rendements modérés à excellents (50-99%). A titre de note, la diminution de la charge catalytique à 0.25 mol% a permis de maintenir un excellent niveau de réactivité pour la réduction de **2a** en **4a** (88%). À nouveau, la présence de groupements attracteurs tels qu'un cyano **4f**, des esters méthylique **4g** et benzylique **4h** ou encore un groupement trifluorométhyle **4i** est bien tolérée (36-85%) tandis que celle de groupements électrodonneurs et l'absence de substitution inhibent totalement la réaction, aucune trace des produits de réduction correspondants **4j-m** n'étant observée dans ces cas. Enfin, la réduction de sels d'ammonium dérivés de la pyrrolidine **7** et de la morpholine **8** a permis d'obtenir le biphenyle correspondant avec des rendements de 52% et 81%, respectivement.

3.2. Couplages radicalaires au départ de sels d'ammonium aromatiques

Après avoir procédé à la réduction des radicaux benzyliques et aryles, nous avons cherché à exploiter ces derniers pour la création de nouvelles liaisons carbone – carbone et carbone – hétéroatome en les piégeant avec différents accepteurs de radicaux connus pour réagir rapidement avec des espèces radicalaires. En effet, le succès du développement de ces couplages

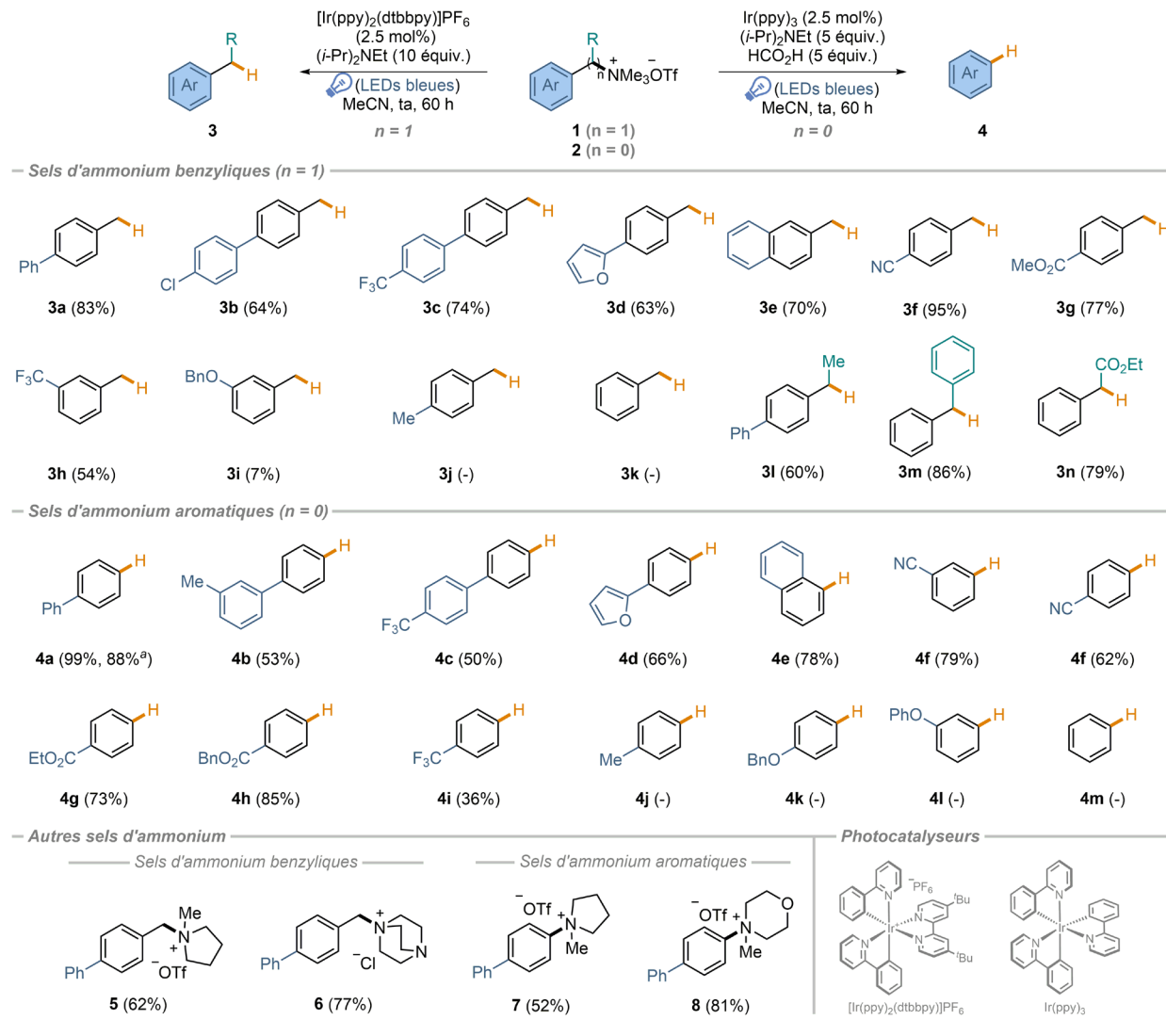


Schéma 1. Hydrodéamination de sels d'ammonium benzyliques et aromatiques : champ d'application. ^aRéaction effectuée avec 0.25 mol% de photocatalyseur.

radicalaires au départ de sels d'ammonium repose sur la capacité des accepteurs de radicaux à piéger les radicaux aryles plus rapidement que le transfert d'un atome d'hydrogène depuis le réducteur sacrificiel ou que leur sur-réduction en anion aromatique [37]. Comme illustré au Schéma 2, différents couplages radicalaires ont ainsi pu être effectués au départ du sel d'ammonium aromatique **2a** tels qu'une réaction d'arylation avec du *N*méthylpyrrole **9**, une réaction d'addition avec du 1,1diphénylethylène **11**, ainsi que des réactions de borylation et de phosphorylation à l'aide de bis(pinacolato)dibore **13** et de phosphite de triéthyle **15**. Dans tous les cas, le couplage est favorisé par rapport à la réduction compétitive, le

biphényle **4a** correspondant n'ayant été observé qu'à l'état de traces.

3.3. Quenching de luminescence (Stern-Volmer)

Après avoir étudié l'activation des sels d'ammonium benzyliques et aromatiques à l'aide de photocatalyseurs d'iridium, nous nous sommes intéressés au mécanisme du clivage de leur liaison C-N par le biais d'études de quenching de luminescence de type Stern-Volmer qui évaluent la diminution de la luminescence d'un photocatalyseur à l'état excité en présence d'une quantité grandissante d'un quencheur. Dans notre cas, ces études ont permis de montrer que

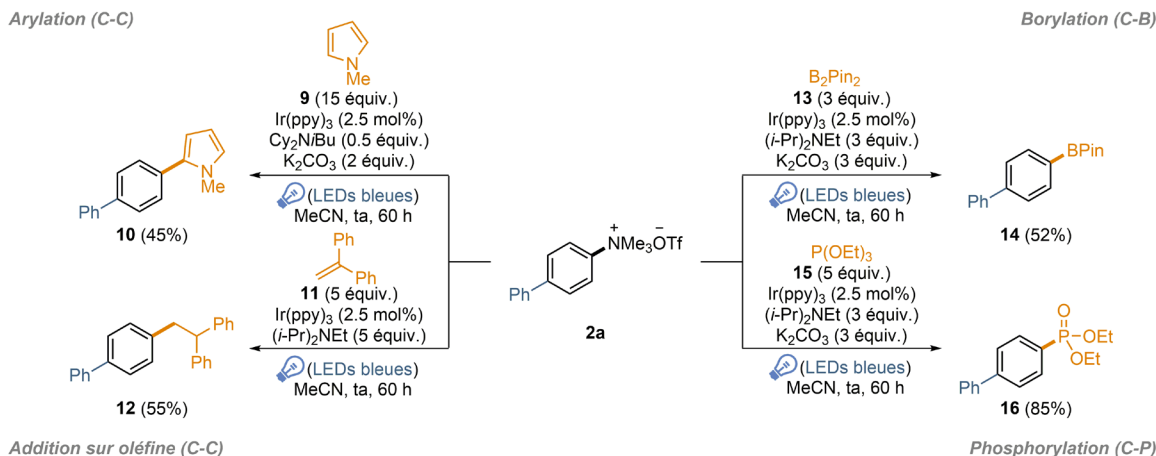


Schéma 2. Couplages radicalaires entre le sel d'ammonium aromatique **2a** et différents accepteurs de radicaux.

les sels d'ammonium benzyliques étaient moins enclins à quencher le photocatalyseur à l'état excité $[\text{Ir}(\text{ppy})_2(\text{dtbbpy})]\text{PF}_6^*$ que la base de Hünig tandis que l'inverse est observé pour les sels d'ammonium aromatiques qui quenchent plus efficacement le photocatalyseur à l'état excité $\text{Ir}(\text{ppy})_3^*$ que la base d'Hünig (Figure 3). Ces résultats suggèrent que des cycles de quenching différents opèrent pour les deux types de sels d'ammonium étudiés au cours de ce travail.

3.4. Détermination des potentiels rédox par voltammetrie cyclique

Afin de rationaliser les différences marquées de réactivité observées pour les différents sels d'ammonium benzyliques et aromatiques, nous nous sommes ensuite attachés à déterminer leurs potentiels rédox par voltammetrie cyclique. Comme illustré à la Figure 3 ci-après, tous les sels d'ammonium présentent des potentiels rédox fortement négatifs allant de -1.70 à -2.47 V vs ECS, ce qui illustre bien la difficulté que représente leur réduction. On remarque également que la substitution des sels d'ammonium a une forte influence sur leur potentiel rédox. En effet, les sels d'ammonium neutres **1k** et **2m** et riches en électrons **1i,j** et **2j-l** sont sensiblement plus difficiles à réduire que les dérivés substitués par des groupements électroattracteurs **1f-h** et **2f,f',g,i**. Les sels d'ammonium substitués par des cycles aromatiques **1a** et **2a** présentent quant

à eux des potentiels rédox intermédiaires, tandis que substituer la position benzylique facilite également la réduction des sels d'ammonium correspondants **1l-n**. Ces tendances sont valables à la fois pour les sels d'ammonium benzyliques et aromatiques et concordent parfaitement avec les profils de réactivité observés lors de l'étude des champs d'application des réactions d'hydrodéamination. L'utilisation de photocatalyseurs d'iridium permet donc d'activer efficacement les sels d'ammonium benzyliques et aromatiques pauvres en électrons et substitués par des groupements aromatiques tandis que les dérivés riches en électrons sont plus difficiles à activer. Finalement, il existe une différence notable entre les potentiels rédox des sels d'ammonium et ceux des photocatalyseurs d'iridium utilisés qui suggère que ces derniers ne devraient pas être suffisamment réducteurs que pour activer la liaison C-N des sels d'ammonium d'intérêt. De telles différences pourraient signifier que les cycles de quenching conventionnels en catalyse photorédox ne sont pas d'application dans le cas présent, même si ceci a déjà été observé avec $\text{Ir}(\text{ppy})_3$, qui a déjà été exploité pour l'activation de composés possédant des potentiels rédox plus bas que -2.0 V vs ECS [38-39]. De plus amples études mécanistiques sont donc nécessaires afin de déterminer avec précision le mécanisme d'activation des liaisons carbone – azote des sels d'ammonium par catalyse photorédox à l'iridium.

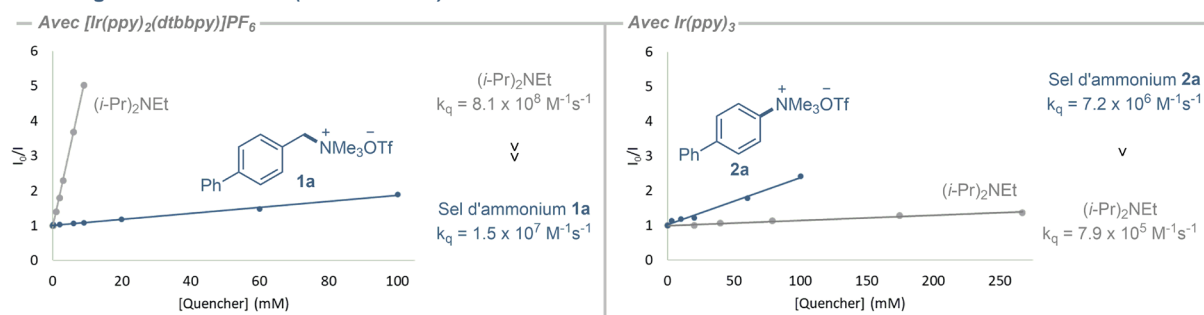
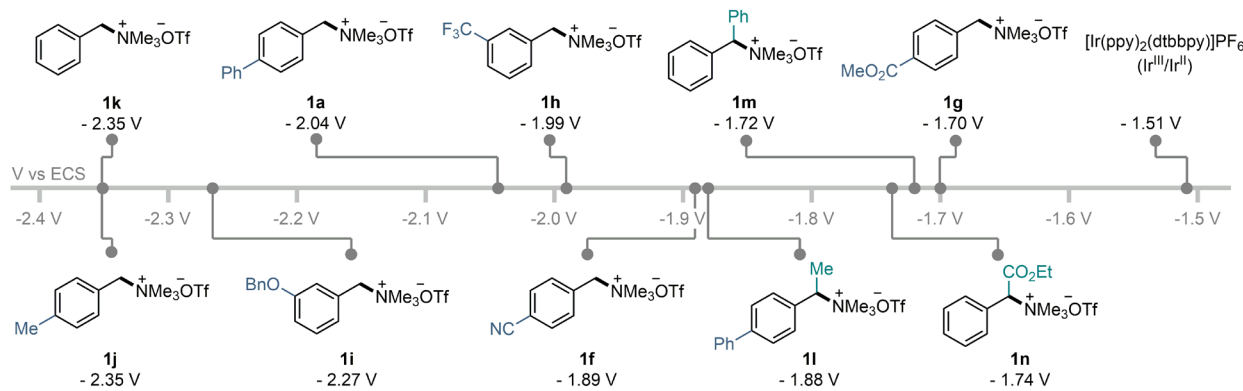
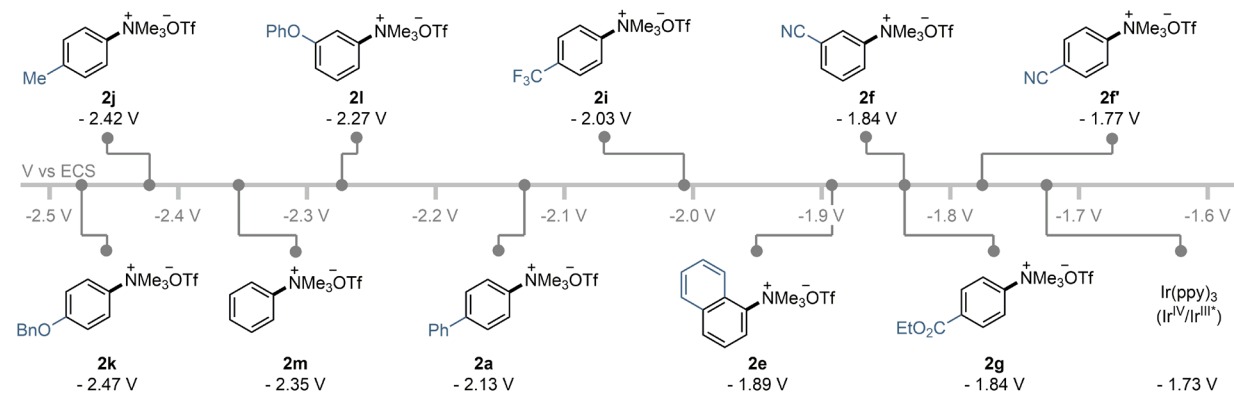
Quenching de luminescence (Stern-Volmer)**Echelle de potentiels rédox de sels d'ammonium benzyliques****Echelle de potentiels rédox de sels d'ammonium aromatiques**

Figure 3. Etudes de quenching de luminescence et échelles de potentiels rédox de différents sels d'ammonium représentatifs.

3.5. Conclusion

Si l'activation de liaisons traditionnellement considérées comme inertes telles que les liaisons C-N ouvre de nouvelles perspectives en synthèse organique moderne, le développement de nouvelles stratégies reste nécessaire afin d'exploiter pleinement les amines en tant que matières premières renouvelables. En chimie radicalaire, de récents progrès ont permis de

faciliter l'utilisation des amines et de certains de leurs dérivés comme précurseurs de radicaux même si plusieurs limitations persistent, limitant de ce fait l'intérêt synthétique des procédés correspondants. Dans ce but, l'utilisation des sels d'ammonium comme précurseurs de radicaux plus attractifs a récemment été décrites et celle-ci permet de pallier certaines limitations tout en ouvrant de nouvelles perspectives dans le domaine.

Au cours de notre étude, nous avons pu décrire l'activation de la liaison C-N au sein de sels d'ammonium benzyliques et aromatiques par catalyse photorédox à l'iridium et leur exploitation dans des réactions d'hydrodéamination et dans des couplages radicalaires permettant la formation de nouvelles liaisons C(sp²)C, C(sp²)B et C(sp²)P [40]. La détermination des potentiels redox d'une série de sels d'ammonium a permis de rendre compte des profils de réactivité observés expérimentalement, ce qui devrait également permettre de mieux prédire la réactivité des sels d'ammonium en conditions réductrices et ainsi faciliter le développement de nouveaux systèmes d'activation dans le futur.

Remerciements

Ce travail a bénéficié de financements provenant du F.R.S.-FNRS, de l'Université libre de Bruxelles (ULB, projet ARC - ENLIGHTEN ME) et du programme EoS (BIOFACT, Projet N° O019618F). L'auteur remercie également le F.R.S.-FNRS pour des mandats de *Charge de recherches* et de *Collaborateur scientifique*, le Dr. J. Annibaletto et le Dr. C. Jacob (ULB) pour leur participation aux travaux de recherche décrits, ainsi que le Pr. G. Evano (ULB).

Références

- [1] V. Froidevaux, C. Negrell, S. Caillol, J.-P. Pascault, B. Boutevin, *Chem. Rev.* **2016**, *116*, 14181.
- [2] K. Ouyang, W. Hao, W.-X. Zhang, Z. Xi, *Chem. Rev.* **2015**, *115*, 12045.
- [3] Q. Wang, Y. Su, L. Li, H. Huang, *Chem. Soc. Rev.* **2016**, *45*, 1257.
- [4] J. García-Cárceles, K. A. Bahou, J. F. Bower, *ACS Catal.* **2020**, *10*, 12738.
- [5] *Encyclopedia of Radicals in Chemistry, Biology and Materials*; C. Chatgilialoglu, A. Studer, Eds.; Chichester, **2012**.
- [6] J. M. R. Narayanan, C. R. J. Stephenson, *Chem. Soc. Rev.* **2011**, *40*, 102.
- [7] C. K. Prier, D. A. Rankic, D. W. C. MacMillan, *Chem. Rev.* **2013**, *113*, 5322.
- [8] A. Kaga, S. Chiba, *ACS Catal.* **2017**, *7*, 4697.
- [9] E. J. Horn, B. R. Rosen, P. S. Baran, *ACS Cent. Sci.* **2016**, *2*, 302.
- [10] S. Möhle, M. Zirbes, E. Rodrigo, T. Gieshoff, A. Wiebe, S. R. Waldvogel, *Angew. Chem. Int. Ed.* **2018**, *57*, 6018.
- [11] C. Galli, *Chem. Rev.* **1988**, *88*, 765.
- [12] D. P. Hari, B. König, *Angew. Chem. Int. Ed.* **2013**, *52*, 4734.
- [13] S. L. Rössler, B. J. Jelier, E. Magnier, G. Dagousset, E. M. Carreira, A. Togni, *Angew. Chem. Int. Ed.* **2020**, *59*, 9264.
- [14] M. A. Ashley, T. Rovis, *J. Am. Chem. Soc.* **2020**, *142*, 18310.
- [15] J. R. Dorsheimer, M. A. Ashley, T. Rovis, *J. Am. Chem. Soc.* **2021**, *143*, 19294.
- [16] D. P. Hari, P. Schroll, B. König, *J. Am. Chem. Soc.* **2012**, *134*, 2958.
- [17] C. H. Basch, J. Liao, J. Xu, J. J. Piane, M. P. Watson, *J. Am. Chem. Soc.* **2017**, *139*, 5313.
- [18] J. B. Washington, M. Assante, C. Yan, D. McKinney, V. Juba, A. G. Leach, S. E. Baillie, M. Reid, *Chem. Sci.* **2021**, *12*, 6949.
- [19] Z.-X. Wang, B. Yang, *Org. Biomol. Chem.* **2020**, *18*, 1057.
- [20] B. Yan, Y. Zhou, J. Wu, M. Ran, H. Li, Q. Yao, *Org. Chem. Front.* **2021**, *8*, 5244.
- [21] C. P. Chernoswky, A. F. Chmiel, Z. K. Wickens, *Angew. Chem. Int. Ed.* **2021**, *60*, 21418.
- [22] A. F. Chmiel, O. P. Williams, C. P. Chernoswky, C. S. Yeung, Z. K. Wickens, *J. Am. Chem. Soc.* **2021**, *143*, 10882.
- [23] C. M. Hendy, G. C. Smith, Z. Xu, T. Lian, N. T. Jui, *J. Am. Chem. Soc.* **2021**, *143*, 8987.
- [24] D.-T. Yang, M. Zhu, Z. J. Schiffer, K. Williams, X. Song, X. Liu, K. Manthiram, *ACS Catal.* **2019**, *9*, 4699.
- [25] J.-J. Brunet, C. Sidot, P. Caubere, *J. Org. Chem.* **1983**, *48*, 1919.
- [26] A. M. Veatch, S. Liu, E. J. Alexanian, *Angew. Chem. Int. Ed.* **2022**, *61*, e202210772.
- [27] X. Kong, L. Lin, Q. Chen, B. Xu, *Org. Chem. Front.* **2021**, *8*, 702.
- [28] A. M. Mfuh, J. D. Doyle, B. Chhetri, H. D. Arman, O. V. Larionov, *J. Am. Chem. Soc.* **2016**, *138*, 2985.
- [29] S. Jin, H. T. Dang, G. C. Haug, R. He, V. D. Nguyen, V. T. Nguyen, H. D. Arman, K. S. Schanze, O. V. Larionov, *J. Am. Chem. Soc.* **2020**, *142*, 1603.
- [30] S. Wang, H. Wang, B. König, *Chem.* **2021**, *7*, 1653.
- [31] M. Li, S. Liu, H. Bao, Q. Li, Y.-H. Deng, T.-Y. Sun, L. Wang, *Chem. Sci.* **2022**, *13*, 4909.
- [32] L. Pan, A. S. Kelley, M. V. Cooke, M. M. Deckert, S. Laulhé, *ACS Sustainable Chem. Eng.* **2022**, *10*, 691.
- [33] X. Kong, Y. Wang, Y. Chen, X. Chen, L. Lin, Z.-Y. Cao, *Org. Chem. Front.* **2022**, *9*, 1288.
- [34] L.-L. Liao, G.-M. Cao, J.-H. Ye, G.-Q. Sun, W.-J. Zhou, Y.-Y. Gui, S.-S. Yan, G. Shen, D.-G. Yu, *J. Am. Chem. Soc.* **2018**, *140*, 17338.
- [35] C. Kerzig, X. Guo, O. S. Wenger, *J. Am. Chem. Soc.* **2019**, *141*, 2122.
- [36] B. Pfund, D. M. Steffen, M. R. Schreier, M.-S. Bertrams, C. Ye, K. Börjesson, O. S. Wenger, C. Kerzig, *J. Am. Chem. Soc.* **2020**, *142*, 10468.
- [37] C. P. Andrieux, J. Pinson, *J. Am. Chem. Soc.* **2003**, *125*, 14801.
- [38] K. A. King, P. J. Spellane, R. J. Watts, *J. Am. Chem. Soc.* **1985**, *107*, 1431.
- [39] J. D. Nguyen, E. M. D'Amato, J. M. R. Narayanan, C. R. J. Stephenson, *Nat. Chem.* **2012**, *4*, 854.
- [40] J. Annibaletto, C. Jacob, C. Theunissen, *Org. Lett.* **2022**, *24*, 4170.

Florian REGNIER^{1,2}, Antoine RILLAERTS^{1,2},
 Vincent LEMAUR¹, Pascal VIVILLE^{2*}, Jérôme CORNIL^{1*}
¹ Laboratory for Chemistry of Novel Materials,
 University of Mons, 7000 Mons, Belgium
² Materia Nova, Research and Development Center,
 7000 Mons, Belgium
 pascal.viville@materianova.be, jerome.cornil@umons.ac.be



A Joint Theoretical and Experimental Characterization of the Rising Star Y6 Acceptor in Organic Solar Cells – From Molecules to Devices

Abstract

For several years, climate changes and energy crisis have pushed the scientific community to develop sustainable and environmentally friendly technologies. This has notably given rise to the field of organic electronics aiming at exploiting organic materials as active layers in devices such as field-effect transistors (OFETs), photovoltaic devices (OPVs) or the well-marketed light-emitting diodes (OLEDs). The OPV technology is considered as a promising candidate to contribute to the energy transition although the devices still need to be improved in terms of performance and stability, especially via the development of new materials. In this context, we report here a joint theoretical and experimental characterization of the highly promising Y6 molecule used as acceptor in the last generation of devices. We demonstrate in particular that the solvent used for depositing the active layer (here chloroform versus chlorobenzene) strongly impacts their morphology, and in turn the solar cell performances.

1. Introduction

Over the past 40 years, climate changes and the resulting energy crisis have been steadily growing [1-3]. This phenomenon has been originating from the Industrial Revolution, a period characterized by

an excessive increase in demand and consumption of energy as well as an extreme dependence on fossil fuels (gas, coal, oil, petroleum) [3-4]. Today, this demand is still increasing mainly due to the population growth and rapid development of technology [2-3]. However, the use of fossil fuels to fulfil this demand generates greenhouse gas emissions, such as the release of carbon dioxide (~35 billion tons in 2021) [5-6] which directly impacts environment and climate [2]. Moreover, fossil fuel resources are becoming limited and are likely to get exhausted soon, thus leading to possible socio-political conflicts, discontinuity or interruption of supply and sudden fluctuations of prices as we are currently facing [2]. On the basis of this emergency, a rethinking of our production methods as well as of our daily energy consumption is undoubtedly necessary to ensure the survival of the human race and all other living species of the planet in an ideally carbon-neutral future.

One well-accepted solution to promote the energy transition is the use of renewable resources. These technologies have the advantages to be sustainable, clean, abundant and to emit limited quantities of CO₂ during their life cycle; they can be easily developed in areas far away from cities and exhibit low operating and maintenance costs compared to more conventional fossil fuel technologies [2]. Among renewable energies, the

solar energy is the most significant exploitable energy source [3,7]. Indeed, the actual available capacity of solar energy on the surface of Earth is estimated at 600 TW [8], which is larger than our annual energy consumption of 13 TW [7-8] and much larger than those estimated for all other renewable technologies, such as hydroelectricity (0.5 TW), geothermal energy (12 TW) or wind energy (2 to 4 TW) [7-8]. Therefore, even if solar energy is intermittent, it represents an inexhaustible and universal energy source which exploited in different ways including solar thermal (e.g., solar tower or solar parabolic trough), bioenergy (photosynthesis), solar photovoltaic or photocatalytic applications [2-3].

1.1. The photovoltaic technology

Solar energy is typically collected with photovoltaic devices (PVs) that convert light into electricity. The physical phenomenon responsible for this conversion is called the “photovoltaic effect” discovered in 1839 by the French physicist Edmond Becquerel [3,9-10]. The original version of PVs, accounting for over 90% of the actual market [3,11], includes monocrystalline or polycrystalline silicon wafers [11-12]. Although their actual conversion yield, called “Power Conversion Efficiency” (PCE or η) reaches 27.6% at the laboratory scale [13], silicon solar cells (Si-SCs) have many drawbacks such as poor light absorption [14-15], high weight due to the large thickness of the layers required to absorb enough light [14-15] and high energy-consuming production steps due to purification processes required to ensure an efficient operation of the devices [14,16]. Such limitations have motivated the scientific community to elaborate other technologies, notably through the development of new alternative materials to substitute silicon in photovoltaic modules. To date, the intensive efforts have led to two additional generations of PV cells: (i) thin-film solar cells in which the dominant materials are amorphous silicon, cadmium telluride (CdTe) or copper indium gallium diselenide (CIGS) and (ii) an emerging category of devices including dye-sensitized solar cells (DSSCs), perovskite solar cells (PSCs) or organic solar cells (OSCs) [11-12].

Organic solar cells integrate semiconducting polymers or small organic molecules in the light absorbing layer [16-18]. They have been receiving an extensive interest due to their numerous advantages including: (i) light weight (~10 times lighter than Si-SCs) [17,19-20], allowing their use on any vertical support; (ii) good mechanical flexibility [17,19] allowing their deposition on any surface (for example, corrugated support or textile); and (iii) the possibility to fabricate semi-transparent devices [20-21]. OSCs can also be produced by simple, solvent-compatible and low-cost processes [17-19] thanks to the high solubility of organic materials in various solvents. Their processing typically carried out by printing techniques (e.g., spin-coating, slot-die, inkjet, roll-to-roll...) [18], can cover large surfaces with a small quantity of material ($\sim 1 \text{ g/m}^2$) [20], while maintaining high efficiencies and limiting the amount of CO₂ emitted during their manufacturing. OSCs are therefore emergent actors for the development of a highly efficient, environmentally friendly and large-scale technology in the field of organic electronics.

1.2. Device architecture and operating principle of OSCs

OSCs are typically made of an organic photoactive layer containing one electron accepting material (typically small molecules referred abusively as n-type in analogy with Si- SCs) and one electron donating material (typically polymers often described as p-type). They are deposited as two juxtaposed layers or as a bulk heterojunction. The active layer is sandwiched between two electrodes, typically aluminium and the transparent and metallic indium tin oxide (ITO) deposited on glass or plastic substrates [18,22-24], see **Figure 1**.

The general working principle of a bilayer solar cells, presented in **Figure 2**, can be divided into 5 main steps: (1) photon absorption and generation of an electron-hole pair, referred to as exciton; (2) exciton diffusion towards the donor-acceptor interface; (3) formation of an interfacial charge-transfer state and its dissociation into free charge carriers; (4) charge transport to the corresponding

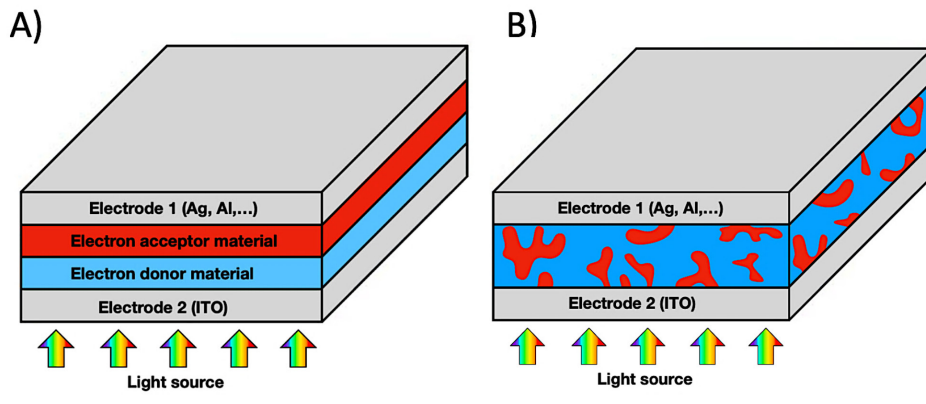


Figure 1: Architecture of (A) a bilayer solar cell and (B) a bulk heterojunction (BHJ) solar cell (B).
The red and blue colors denote respectively the acceptor and donor material.

electrodes; and (5) charge collection at each electrode [25-27]. To efficiently convert light into electricity and achieve high performances, organic solar cells should meet several requirements in order to optimize each of these steps.

The use of a single organic material does not allow for the generation of a photocurrent. Indeed, the high stability of the excitons formed within organic materials makes their dissociation difficult under ambient conditions. The binding energy of excitons (E_b) results from the strong Coulomb attraction between the photogenerated hole and electron. Due to the low dielectric constant (ϵ_r) of organic materials, typically

between 2 and 4, E_b is typically larger than 0.3 eV in semiconducting polymers and can reach up to 1 eV in small molecules due to charge spatial confinement in a small volume [28-29].

The binding energy is thus much higher than the thermal energy at room temperature (~25 meV), thus preventing the dissociation of excitons within the bulk of a single organic material [28-29]. This is why it is necessary to introduce a second organic material in the active layer with a proper positioning of the HOMO and LUMO levels of the two components to promote free charge carrier generation [28,30]. The donor molecule will be characterized by a smaller

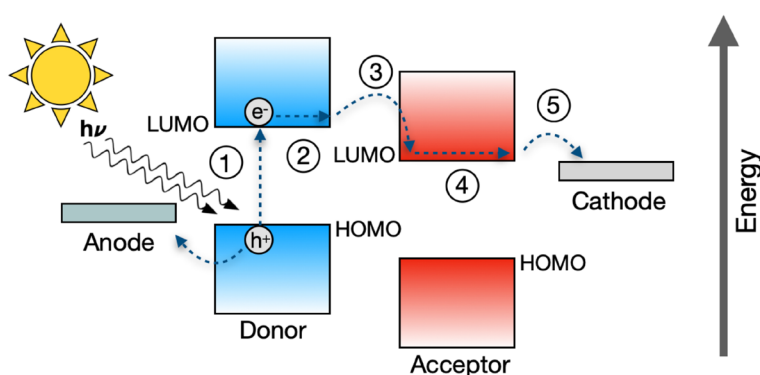


Figure 2: General working principle of a bilayer solar cell (h^+ stands for hole and e^- for electron).

ionization potential (lower HOMO level) and the acceptor by a stronger electron affinity (deeper LUMO) [25-28]. Therefore, if the exciton is generated on the donor compound, the energy difference between the LUMO of the acceptor and that of the donor (ΔE_{LUMO}) must be large enough to exceed the Coulombic attraction and ensure a photoinduced electron transfer, but not too large to avoid the loss of too much energy. Similarly, for an excitation on the acceptor, the photoinduced hole transfer is favorable if the energy difference between the HOMO of the donor and the HOMO of the acceptor (ΔE_{HOMO}) is strong enough to overcome the binding energy of the exciton, as figured out in **Figure 3**.

Although bilayer solar cells are the simplest to produce, their architecture endows only one planar D-A (donor-acceptor) interface for exciton dissociation, leading to cut short efficiencies [22,28,30]. Indeed, due to its short lifetime (< 1 ns), the diffusion length of an exciton is typically limited to a few tens of nanometers [22,25,28] and only excitons generated near the D/A interface can contribute to the charge generation [28]. This major drawback has led to the concept of bulk heterojunction (BHJ) [18,25,28] in

which the active layer can be described as an interpenetrating network of donor and acceptor materials at the nanoscale [22,25]. Accordingly, most of the generated excitons can thus rapidly reach an interface before their recombination to be dissociated into free charge carriers that will then be transported through percolation pathways toward the respective contacts for collection [22,25]. On the negative side, this structure requires a precise control of the morphology to reach the most appropriate phase separation [22,25], which is still a huge current challenge.

In the BHJ device structure, thin inorganic or organic intermediate layers can be introduced between the active layer and electrodes to facilitate charge transport and charge collection, as shown in **Figure 4** [22,25,31-33]. These extra layers allow avoiding direct contact between the photoactive material and electrode, thus preventing exciton recombination at the contacts [32-33] and dictate the charge collection direction (i.e., polarity of the device) by blocking selectively holes at the cathode and electrons at the anode [22,24,32]. Two architectures are actually conceivable: the conventional or direct structure in which electrons are collected at the aluminium electrode and the

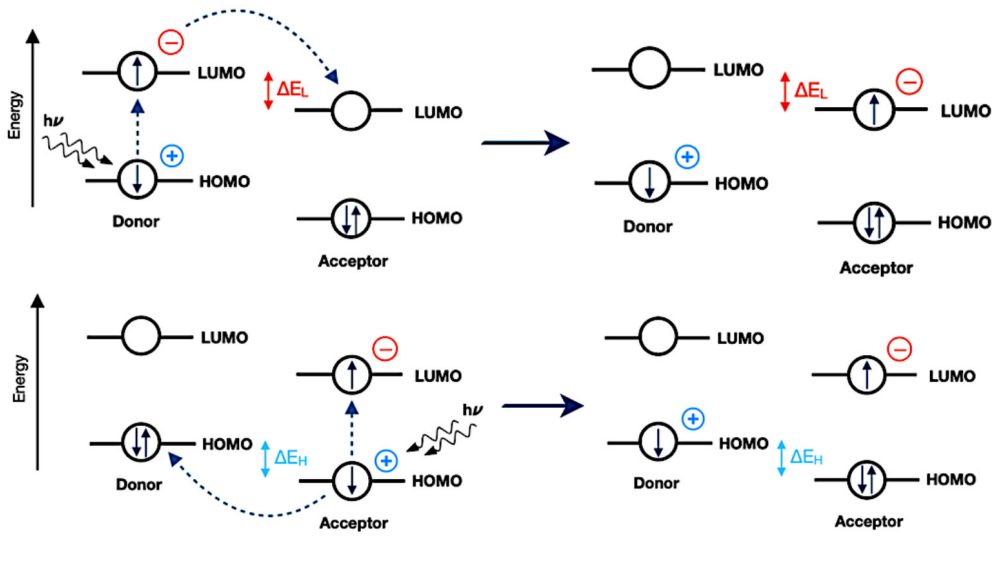


Figure 3: Schematic representation of photoinduced electron transfer (upper figure) and photoinduced hole transfer (lower figure) when the exciton is formed on the donor or on the acceptor respectively. In both cases, an interfacial charge transfer state is created with a hole on the HOMO of the donor and an electron on the LUMO of the acceptor.

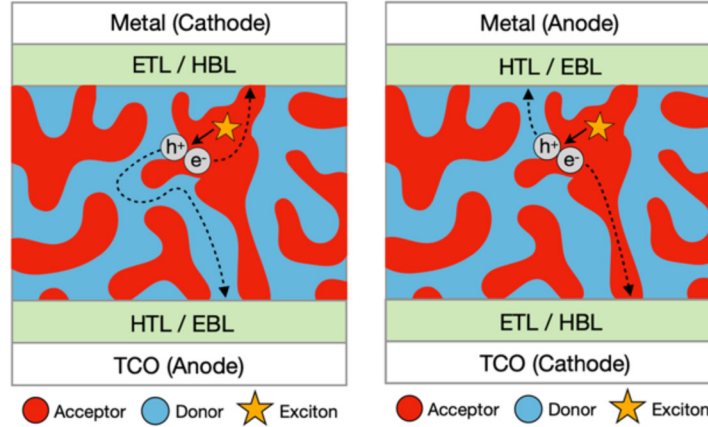


Figure 4: Architecture of conventional (left figure) and inverted (right figure) BHJ organic solar cells. HTL [HBL] denotes Hole Transport [Blocking] Layer and vice versa for electrons.

inverted structure in which electrons are collected at the ITO contact [23]. The blocking layers also prevent damaging chemical reactions or metallic ions diffusion at the electrode/organic interface [22,33-34], thus helping to increase the stability and hence lifetime of the devices. It is worth stressing that the choice of interlayers is limited to a few materials because these must offer simultaneously good charge transport properties, adapted electronic level matching at the photoactive layer/electrode interface, good chemical stability and high transparency to the visible solar irradiation [22,24]. The widely-used hole blocking layers (HBLs) / electron-transporting layers (ETLs) are LiF, TiO_x, ZnO and SnO₂ while electron-blocking layers (EBLs) / hole-transport layers (HTLs) are often WO₃, V₂O₅, MoO₃ and poly(3,4-ethylenedioxythiophene) polystyrene sulfonate (PEDOT:PSS) [3,23-25,31].

1.3. Device characterization

The photovoltaic performances are estimated from current density-voltage (J(V)) curves obtained both under illumination and in the dark, see **Figure 5** [3,30].

By convention, the illuminated curve must be recorded under 1 sun Air Mass 1.5 (AM~1.5 1000 W/m²) conditions [8,30,35-36] in which the light source simulates the sun irradiation on Earth at an angle of about 48° from the zenith [30,36].

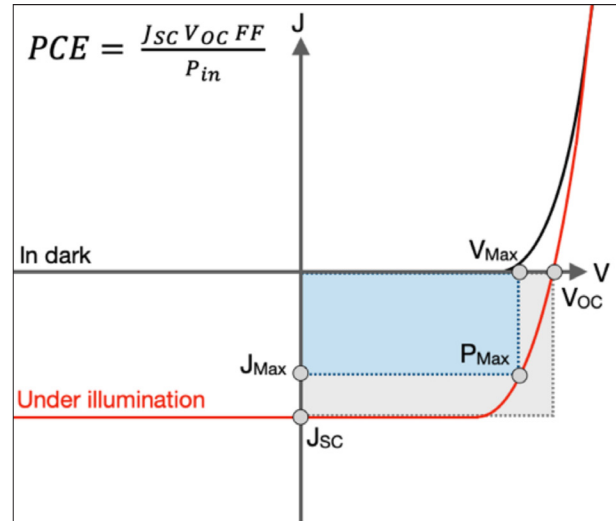


Figure 5: Typical current density-voltage (J(V)) curves obtained from OSCs characterization. The illuminated and dark curves are plotted in red and black, respectively.

From J(V) curves, it is possible to extract the power conversion efficiency, denoted PCE [16,30] expressing the amount of electrical power (P_{out}) produced by the solar cell relative to the power of the incident light radiation (P_{in}) [16,30]. P_{out} is given by the product of three parameters namely the short-circuit current (J_{SC}), open-circuit potential (V_{OC}) and fill factor (FF) [16,30]. Obtaining high efficiency OSCs requires maximizing these three key parameters (J_{SC} , V_{OC} , FF).

The short-circuit current (J_{SC}) corresponds to the current density that flows through the illuminated solar cell when no electrical potential is applied

[22,28,30]. J_{SC} depends on the efficiency of light absorption, the mobility of charge carriers and is reduced by charge recombination phenomena [16]. The open-circuit potential (V_{OC}) represents the value of the bias at which there is no current in the device [28,30]. The maximum value of V_{OC} matches the energy difference between the LUMO of the acceptor and the HOMO of the donor [18,33,37], but is further reduced with the charge recombination phenomena occurring in the active layer. The fill factor (FF) is defined as the ratio of the maximum power actually delivered by the device (area of the blue rectangle, $P_{max} = J_{max} \times V_{max}$) and the ideal maximum power output (area of grey rectangle) obtained when $P_{max} = J_{SC} \times V_{OC}$, see **Figure 5** [30,38]. This FF parameter is affected by two types of resistance across the device: the series resistance (R_S) and the parallel resistance (R_{Sh}) [22,37]. R_S depends on the interface contact resistance between the stacking layers and the bulk resistance of each material [39]. This resistance can be estimated from the slope of the $J(V)$ curve near V_{OC} and must be as low as possible ($R_S \rightarrow 0$) [37,39]. The R_{Sh} parameter is impacted by any current leakage from the edge of the cell and from pinholes in the film or by the presence of energy traps typically associated to energetic disorder among the transport levels. This resistance should

be as high as possible ($R_{Sh} \rightarrow \infty$) to increase FF and is estimated from the slope of the $J(V)$ curve near the J_{SC} [37,39].

1.4. The birth of NFA molecules

The first generation of OSCs was based on active layers including donor polymers, such as the well-known poly(3-hexylthiophene) (P3HT), combined to the prototypical fullerene-type acceptor molecule (FAs) 1-(3-methoxycarbonyl) propyl-1-phenyl[6,6]C₆₁ (PC₆₁BM) [17,40-41]. Although PCBM presents interesting isotropic charge transport properties and a high electron affinity [17], devices involving them exhibited limited conversion efficiency, between 5% and 11% [40-41], mainly due to the poor absorption properties of fullerenes, chemical stability problems and morphological instability linked to the spherical shape of the fullerene compounds [19,26,40,42]. Tremendous molecular design efforts have thus been carried out to develop new classes of non-fullerene acceptor molecules (NFAs). Among them, the most extensively studied compounds feature an A-D-A structure as represented by the ITIC-series that appeared in 2015, as well as an A-D-A'-D-A-type structure such as in the Y-series developed in 2019 (**Figure 6**) [17,19].

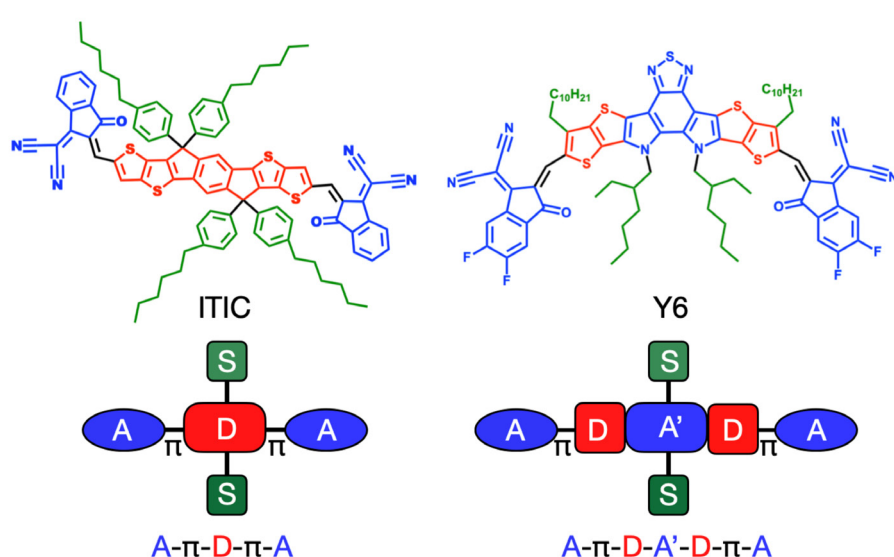


Figure 6: Molecular structure of ITIC and Y6 NFA. The distinctive domains are highlighted: acceptor unit (blue), donor unit (red) and side chains (green).

Today, NFAs have pushed the power conversion efficiency (PCE) beyond 15% at the laboratory scale after full device optimization and adequate choice of additives [19,43-44]. This boost in photovoltaic performances can be undoubtedly attributed to the key assets of NFAs compared to FA derivatives, such as a significant absorption of the solar emission or a very modular structure, which allows for fine tuning the solid-state packing and electronic/optical properties driving the efficiency of the different steps in solar conversion [19,26,40,42,45]. Developing new materials with enhanced performance definitively requires now the establishment of structure-properties-device performance that are often overlooked when searching for formulations yielding the highest power conversion efficiency.

In this paper, we contribute to this endeavor by reporting a fundamental study of the electronic, optical and morphological properties of the molecular electron acceptor Y6 currently considered as a rising star in the field. By combining theoretical modelling, experimental characterizations and device fabrication, we highlight some factors explaining why this NFA material leads to higher conversion efficiencies compared to the pristine FA compounds and

propose different guidelines for the development of new compounds.

2. Results and discussion

2.1. Theoretical modelling

The first part of our study starts with a theoretical investigation of the structural, electronic and optical properties of the Y6 molecule. We performed here quantum-chemical calculations at the DFT (Density Functional Theory) level using the LC- ω HPBE functional and a 6-31G(d,p) basis set [46-48], as implemented in Gaussian 16 (revision A.03) [49]. All alkyl side chains in the molecular structure were replaced by methyl groups (-CH₃) to reduce calculation time [50-51]. Changing the length of the side chains does not affect the properties of isolated molecules and should not strongly impact the structural properties of the conjugated central core inferred in presence of the methyl groups. The optimized molecular geometry obtained with an adjusted ω value of 0,1068 Bohr⁻¹ is presented in **Figure 7**. The molecule adopts a U-shaped geometry with a permanent dipole moment of 1.7 Debye along the Z-axis. This structural change, compared to the previous S-shaped ITIC-series

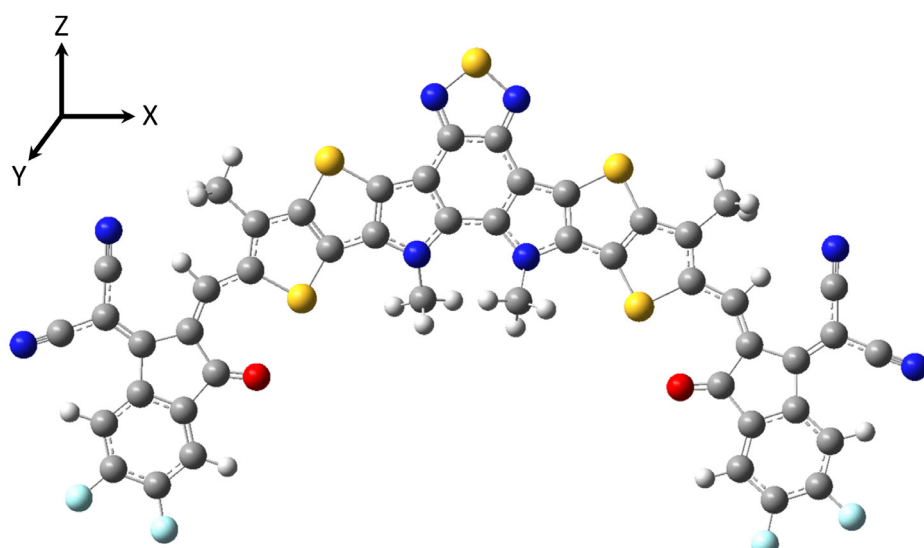


Figure 7: Optimized structure of Y6 obtained from LC- ω HPBE/6-31G(d,p) DFT calculations.

with no dipole, is likely to impact intermolecular interactions between molecules in the condensed phase (i.e., the molecular packing) and hence the charge transport properties [26,52]. In spite of a slight central twist of 12.7° induced by steric hindrance between the inner alkyl groups, Y6 exhibits a pronounced molecular flatness which is favorable to extent π -electron delocalization over the molecular backbone.

The shape of the frontier orbitals (FOs) has also been computed, while considering solvent effects via a Polarizable Continuum Model (PCM); we consider here chloroform ($\epsilon = 4.71$) and chlorobenzene ($\epsilon = 5.69$) commonly used in the literature due to their excellent dissolution ability of NFAs [53-55]. Since the results obtained are similar in both solvents, the following discussion is only focused on the results obtained in chloroform. As shown in **Figure 8**, the LUMO of Y6 is completely delocalized all along backbone while its HOMO is mostly localized on the center [51,56].

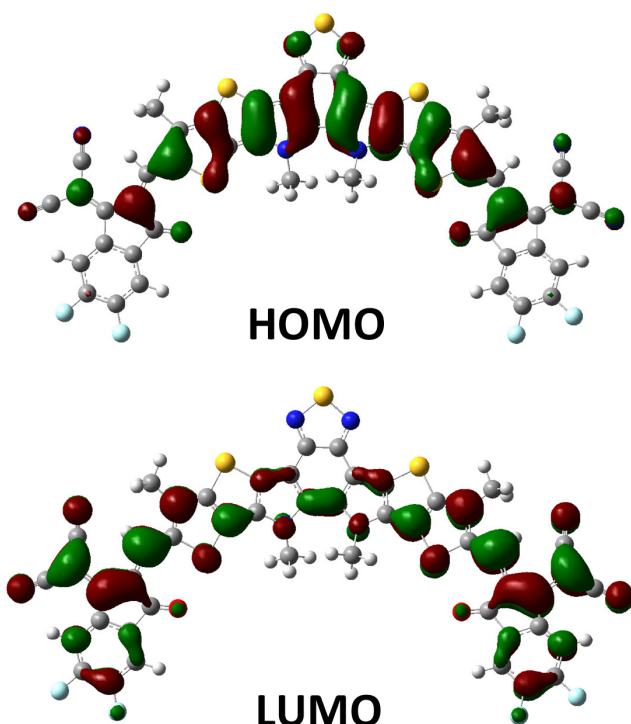


Figure 8: HOMO/LUMO wavefunction distribution in Y6 obtained from LC- ω HPBE/6-31G(d,p) DFT calculations taking into account solvent effect of chloroform. The wavefunction sign is represented by red (positive) and green (negative) colors.

This high delocalization of the LUMO level is an interesting feature to promote intermolecular electron transport between adjacent molecules in the condensed phase.

A Mulliken population analysis, presented in **Figure 9**, has been conducted to study the donor/acceptor character of the molecular domains.

The terminal groups, thienothiophene core units and the BT group fused to the neighboring pyrroles, as highlighted in **Figure 10**, have a respective charge of -0,4 |e|, +0,6 |e| and -0,2 |e|. Moreover, the Mulliken analysis points to attractive interactions between the positive charge on the sulfur atom of one thiophene of the core (+0.38 |e|) and the negative charge on the adjacent oxygen atom located on the terminal group (-0.47 |e|). This S-O coulombic attractive interaction ($d_{S-O} \sim 2.7 \text{ \AA}$) might trigger a conformational blocking favoring further the coplanarity of the molecule [44,57].

In order to investigate the impact of end-group halogenation on the optoelectronic properties in existing Y derivatives, similar theoretical calculations were carried out on the optimized structures of the non-halogenated and chlorinated derivatives of Y6, respectively Y5 (BTP) and Y7 (BTP-4Cl). The optimized value of ω is also 0,1068 Bohr¹ for both molecules. Halogenation of terminal groups does not significantly impact the electronic gap ($E_{\text{Gap}} = E_{\text{HOMO}} - E_{\text{LUMO}}$) as illustrated in **Figure 11**, or frontier orbital localization whatever the solvent employed but lowers progressively the energy of the frontier electronic levels when going from Y5 to Y7. Therefore, the terminal group halogenation appears to be an effective strategy to modify the V_{OC} parameter in OSC devices without impacting the absorption spectra of the molecules.

We have finally simulated the absorption spectrum of Y6 and its derivatives in chloroform and chlorobenzene, see **Figure 12**. All graphs are plotted with a full width at half-maximum (FWHM) of 0.25 eV. In spite of the small permanent dipole moment, an interesting observation is the lack of solvatochromism effect (shift of the lowest absorption band by only 6 nm~0.02 eV between

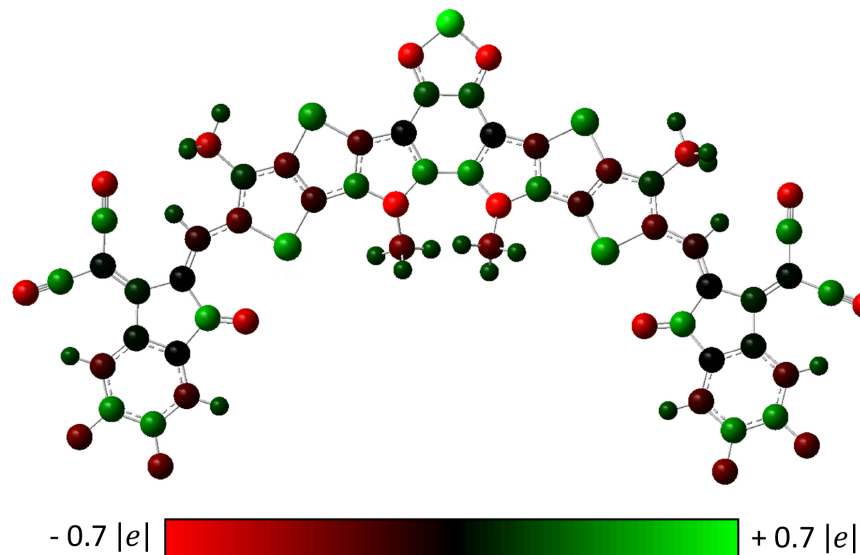


Figure 9: Mulliken population analysis for the Y6 molecule, as obtained at the LC- ω HPBE/6-31G(d,p) DFT level.

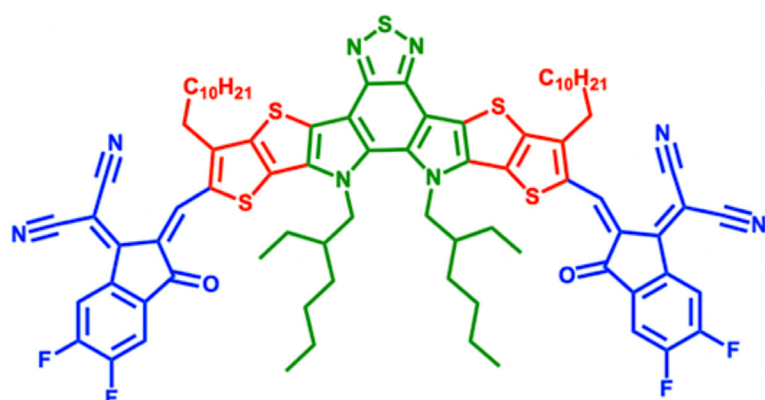


Figure 10: Terminal groups (blue) and thienothienophene core units (red) and BT group fused to the neighboring pyrroles (green) on Y6 molecule.

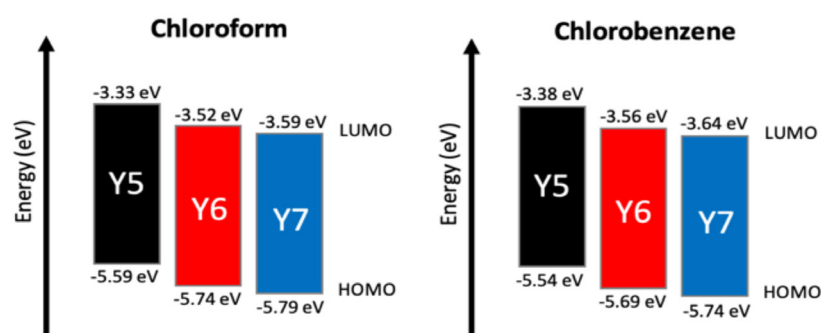


Figure 11: HOMO and LUMO energies obtained from LC- ω HPBE/6-31G(d,p) DFT calculations for Y5, Y6 and Y7 in chloroform (left figure) and chlorobenzene (right figure).

the two solvents) which points to a weak impact of solvent on the optical transitions of the molecules. As expected from the previous considerations, the halogenation of the terminal group has a minimal impact on the optical band gap whatever the solvent used. Indeed, the lowest optical absorption band, corresponding to a transition between the ground state (S_0) to the first excited state (S_1), is located at 615 nm (2.01 eV), 625 nm (1.98 eV) and 635 nm (1.95 eV) for Y5, Y6 and Y7 in chloroform while they lie at 621 nm (2.00 eV), 631 nm (1.97 eV) and 641 nm (1.93 eV) in chlorobenzene, respectively. The calculated molar absorption coefficient (ϵ_λ) is about $1 \cdot 10^5 \text{ M}^{-1} \text{ cm}^{-1}$ for each derivative, denoting the very good absorption properties of these compounds compared to fullerene derivatives ($\epsilon_\lambda < 0.5 \cdot 10^5 \text{ M}^{-1} \text{ cm}^{-1}$) [58]. An overlap factor (ϕ_s) between the hole density (ρ_h) and electron density (ρ_e) associated to first excited state (S_1), mostly described by a HOMO \rightarrow LUMO transition, has been determined to be 0.62 [56,59]. This points to a good compromise between the charge-transfer state character of S_1 ($\phi_s \rightarrow 0$) which facilitates exciton dissociation and a local character ($\phi_s \rightarrow 1$) required for efficient optical absorption [59].

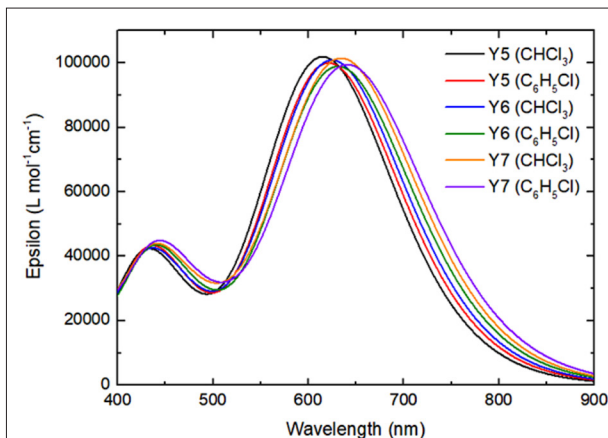


Figure 12: Simulated absorption spectra obtained from TD-DFT/LC- ω HPBE/6-31G(d,p) calculations for Y5, Y6 and Y7 in chloroform and chlorobenzene.

2.2. Optical properties

The experimental UV-visible normalized absorption spectra of Y6 as well as the electron donor polymer PM7 in both host solvents are presented in **Figure 13**.

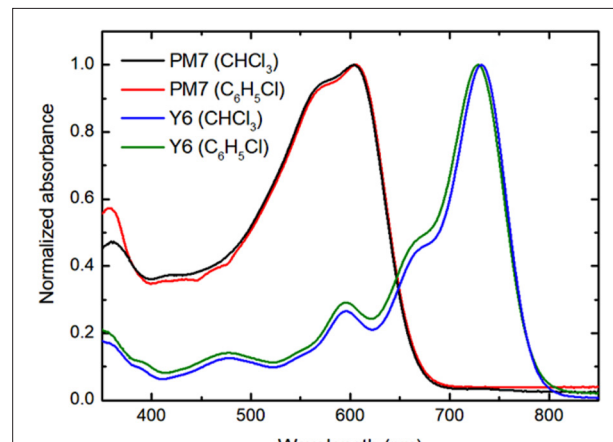


Figure 13: Normalized absorption spectra of Y6 and PM7 in CF and CB solution ($C = 6.25 \cdot 10^{-3} \text{ mg/mL}$).

The absorption maxima are located at 604 nm (2.05 eV) and 732 nm (1.69 eV) for PM7 and Y6 respectively in chloroform [60-61] while they lie at 605 nm (2.05 eV) and 729 nm (1.70 eV) in chlorobenzene, thus reflecting the absence of solvatochromism, as predicted by our theoretical study. From Beer-Lambert's law ($A_\lambda = \epsilon_\lambda \cdot L \cdot C$) [62-63] with the absorbance value at a given wavelength, L the optical path length (cm) and C the molar concentration of absorbing species in solution (mol L⁻¹ or M), the molar absorption coefficients (ϵ_{\max}) at λ_{\max} are determined to be $1.75 \cdot 10^5 \text{ M}^{-1} \text{ cm}^{-1}$ for Y6, in deep consistency with the theoretical estimates yielding values around $10^5 \text{ M}^{-1} \text{ cm}^{-1}$.

UV-Vis spectroscopy analyses on PM7 and Y6 thin films on glass substrate, see **Figure 14**, show a red-shifted absorption compared to the spectra obtained in solution.

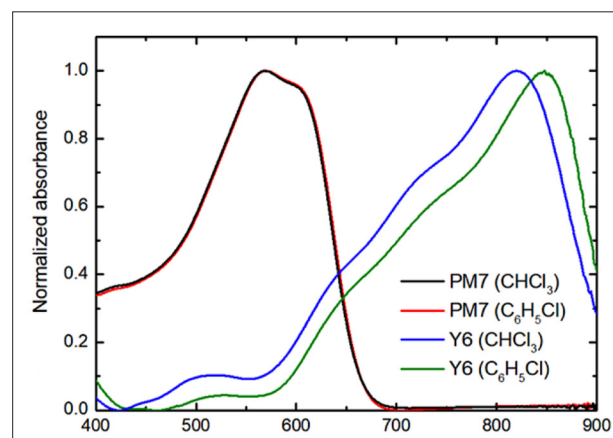


Figure 14: Absorption spectra of PM7 and Y6 films prepared from chloroform and chlorobenzene.

For the PM7 polymer, the $S_0 \rightarrow S_1$ absorption peak is shifted by 3 nm (0.01 eV) in both solvents, while this shift is more pronounced in the case of Y6 with the absorption peak in film located at 819 nm in chloroform (shift ~ 0.18 eV) and 848 nm in chlorobenzene (shift ~ 0.24 eV). The unusually large bathochromic shift observed in the case of Y6 is likely to originate from pronounced $\pi\text{-}\pi$ and/or electrostatic interactions [51,61]. From the formula $\alpha = (\frac{1}{d}) \ln (\frac{1}{T})$, where d represents the film thickness (cm) and T the transmittance [64], the average absorption coefficient (α) in the neat films of Y6 is estimated to be $2.81 \cdot 10^5$ cm $^{-1}$. Such a high absorption coefficient and the high complementarity with the PM7 polymer absorbing in the 600 nm-900 nm range are highly beneficial to maximize the collection of photons in the visible range of wavelengths of the solar spectrum, and hence to increase the value of the J_{SC} parameter [26,51].

2.3. Morphological properties

The surface morphology of non-annealed PM7 and Y6 thin films prepared from the two host solvents as well as of non-annealed PM7:Y6 blend in the [1:1] weight ratio typically used in the active layer was investigated by Atomic Force Microscopy (AFM). The surface of the PM7 film, shown in **Figure 15**, exhibits a similar smoothness in both solvents, with the presence of 30-70 nm-long fiber-like aggregates [65-66].

The root-mean-square surface roughness (R_q) is 1.0 nm and 0.6 nm in chlorobenzene (CB) and chloroform (CF), respectively. Concerning the Y6 neat films, see **Figure 16**, large grains with a size between 40 nm and 110 nm are visualized with both solvents. More aggregation effect is observed in the case of the CB-processed film, translating to a higher R_q value of 5.1 nm compared to CF-processed film with $R_q = 2.8$ nm; this is mostly likely due to a lower solubility of Y6 in CB.

AFM image of a 100-nm PM7:Y6 [1:1] blend, see **Figure 17**, shows different morphologies as a function of the solvent used for their processing. The films prepared from CB exhibit a granular morphology similar to Y6 films. A high R_q of 4.7 nm points to strong aggregation of the Y6 molecules in the mixture. This large domain separation is detrimental for exciton dissociation in the device [43,65]. In contrast, a 100-nm thin film of PM7:Y6 [1:1] prepared from CF shows a morphology quite similar to that of PM7 films alone without grain formation. The R_q is significantly reduced down to 0.9 nm, thus attesting of the good miscibility of the two components.

2.4. Device fabrication and characterization

To evaluate the photovoltaic performances of the 100 nm-thick PM7:Y6 [1:1] active layer deposited from chlorobenzene or chloroform, a series of non-optimized OSCs with an inverted device

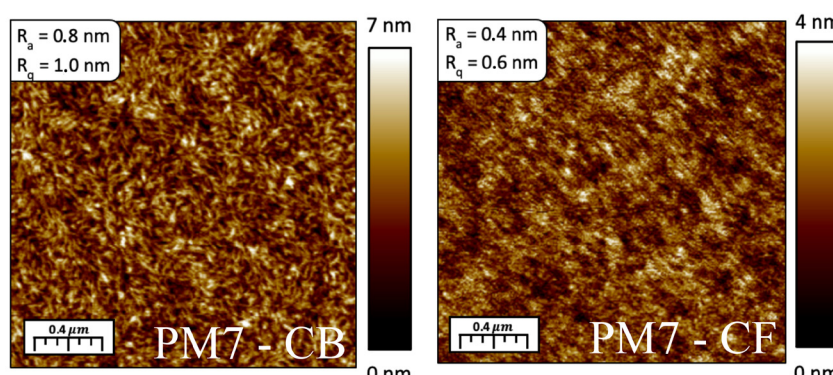


Figure 15: AFM images ($2 \times 2 \mu\text{m}^2$) for PM7 pure films prepared from chlorobenzene (left) and chloroform (right). Their thickness are 150 nm and 170 nm, respectively.

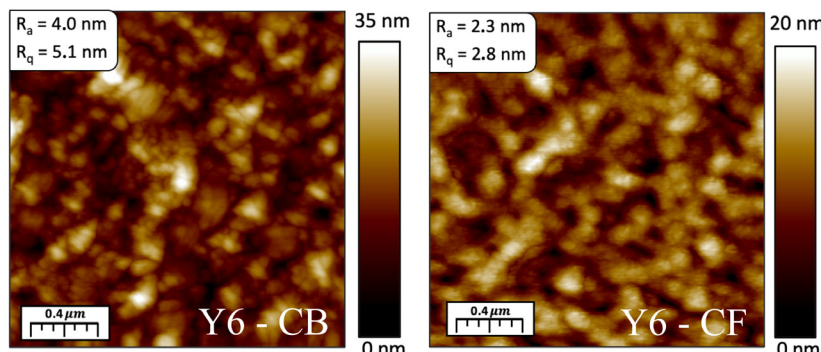


Figure 16: AFM images ($2 \times 2 \mu\text{m}^2$) for neat films of Y6 prepared from chlorobenzene (left) and chloroform (right) solutions. Their thickness is 60 nm for Y6 in chlorobenzene and 90 nm in chloroform.

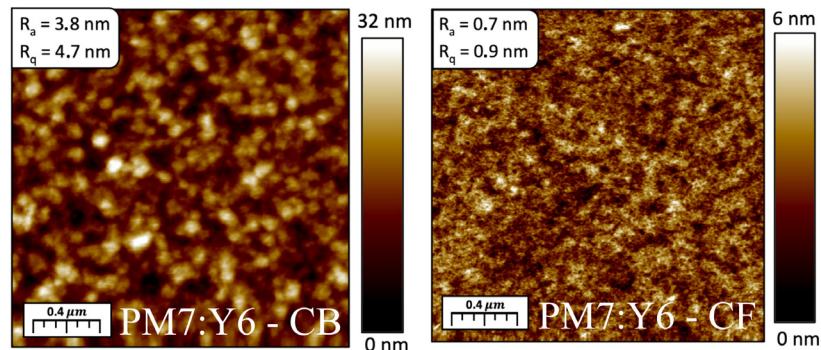


Figure 17: AFM images ($2 \times 2 \mu\text{m}^2$) for blend films of PM7:Y6 prepared from chlorobenzene (left) and chloroform (right) solutions. Their thickness is 105 nm in chlorobenzene and 98 nm in chloroform.

architecture of the type Glass/ITO/Al/SnO₂/Active layer/MoO₃/Al were fabricated and characterized. In this device architecture, deposition of a thin Al layer on the ITO electrode allows for a reduction of the series resistances (R_s) of the devices. The SnO₂ HBL is deposited from a solution containing 0.5 mL of stock solution (2.5 wt% crystalline SnO₂ diluted in butanol) added in 2.6 mL of butanol. This solution was deposited by spin coating at a rotation speed of 3000 rpm for 30 seconds and annealed on a hot plate for 30 min at 150°C. The active layer was spin-coated in both solvents under inert conditions (Nitrogen Glovebox) at a speed of 1500 rpm during 60 seconds and annealed at 100°C for 10 min. The MoO₃ EBL was deposited by thermal evaporation as well as the Al counter electrode. All manufacturing steps (A), the energy diagram of the device (B) [25,44,67-68] and the thickness of each layer (C) are shown in **Figure 18**.

Table 1 summarizes the main characteristics of the fabricated solar cells with an active illuminated zone of 2.56 mm², as systematically averaged over 5 devices (D_x with $x = 1, 2, \dots, 8$) built from the same active layer (see red squares in **Figure 18-A**). Devices made of PM7:Y6 [1:1] deposited from chloroform show the highest performances with an averaged J_{sc} of 14.04 mA/cm², V_{oc} of 0.87 V and FF of 56.46 % leading to a PCE of 6.91 %. When using the chlorobenzene, we obtain a much lower current density of 10.43 mA/cm² but a higher FF of 61.44 %, leading together to a lower PCE of 5.25 %. The significant drop in J_{sc} can be mainly attributed to the granular morphology associated to a lower solubility of Y6 in chlorobenzene. The domain sizes (~ 50 to 150 nm) are indeed larger than the average exciton diffusion length (around 10-20 nm) [22], and hence not favorable for the exciton dissociation process and free carrier

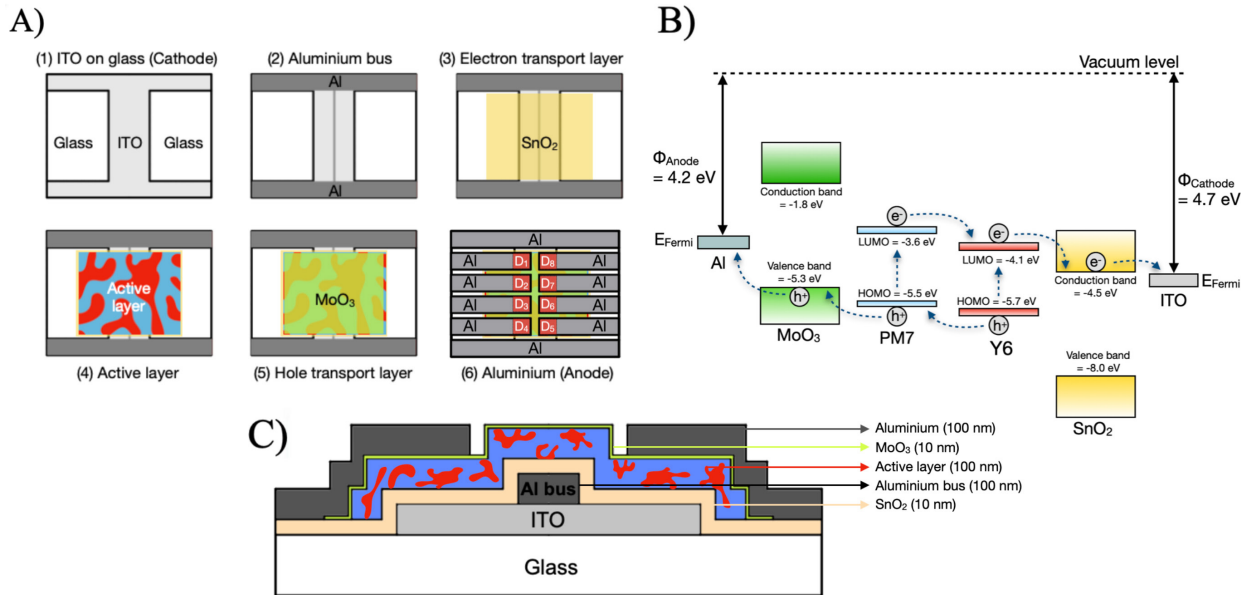


Figure 18: Manufacturing steps for the fabrication of the ITO/Al/SnO₂/PM7:Y6/MoO₃/Al of the eight devices D₁ → D₈ in parallel (A), energy diagram of the electronic structure of the different layers illustrating the device operation from the charge generation to the charge collection (B) and side view (C) of the inverted OSCs device.

generation. The V_{OC} value is conserved around 0.8 V, indicating that the morphology changes do not drastically affect the efficiency of the charge recombination processes.

All blends yield small values of series resistances (R_{Series}) both in the dark and under illumination, thus pointing to good charge extraction and electrical contacts in the device. The slightly lower values in the case of chlorobenzene reflect a lower interface resistance between layers in the devices or a lower bulk resistance in the active blends [39]. Concerning the shunt resistances (R_{Sh}), all blends present a quite high value which points to the absence of significant leakage

currents in the dark [39]. Under illumination, these values sharply decrease around 400-500 Ohm cm²: this likely originates from the presence of energetic disorder (and hence charge carrier traps) that defines specific percolation pathways and prevent a homogeneous extraction of the charges from the active layer [39].

3. Conclusion

To sum up, we performed a combined theoretical and experimental study of the structural, optoelectronic and morphological properties of the widely used NFA Y6. The theoretical exploration points to a high LUMO delocalization,

Active layer [1:1]	Host solvent	J _{SC} (mA/cm ²)	V _{OC} (V)	FF (%)	R _{Serie Light} (Ohm cm ²)	R _{Serie Dark} (Ohm cm ²)	R _{Shunt Light} (Ohm cm ²)	R _{Shunt Dark} (Ohm cm ²)	Morphology	PCE (%)
PM7:Y6	CHCl ₃	14.04 +- 0.50	0.87 +- 0.01	56.46 +- 0.76	1.54 +- 0.17	1.60 +- 0.19	405.4 +- 10.36	46342.80 +- 20219.76	Filaments	6.91 +- 0.27
PM7:Y6	C ₆ H ₅ Cl	10.43 +- 0.41	0.82 +- 0.01	61.44 +- 0.92	0.70 +- 0.07	0.70 +- 0.07	532.20 +- 29.85	14708.80 +- 9820.29	Grains	5.25 +- 0.19

Table 1: Solar cell parameter values averaged over 5 devices on a single substrate.

in spite of the A-D-A'-D-A structure, which should favor intermolecular charge transport properties. The theoretical results also indicate that the halogenation of the terminal groups constitutes a very good strategy to modulate the open-circuit potential in OSCs without strongly impacting the absorption signature of NFAs. The comparison of simulated spectra in two solvents widely used experimentally (CF and CB) evidences a negligible solvatochromism effect on optical transitions, which has been further confirmed by experimental spectra. Spectroscopy analyses of Y6 films show an unexpectedly large bathochromic shift compared to solution, most probably as a result of pronounced π - π and/or electrostatic interactions in the solid state, whatever the host solvent used. Moreover, the high absorption coefficients of Y6 and its complementary with PM7 are highly beneficial to improve the J_{SC} parameter and by extension the PCE of OSCs. Concerning the morphology investigations of Y6 films, large grains are visualized from both solvents, but the higher roughness measured for CB films suggests that Y6 is less soluble in this solvent. A similar grain morphology is observed for the PM7:Y6 blend deposited from CB whereas a filament-like morphology is displayed in CF. A granular morphology in the PM7:Y6 blend is detrimental for the exciton dissociation processes, leading to lower values of J_{SC} and by extension to a lower PCE, as confirmed by the device characteristics. Altogether, this work has highlighted the high potential of the Y6 NFA for organic solar cells and in particular the importance of carefully choosing the solvent used for processing to optimize the morphology of the active layers, which plays a crucial role in defining the OSC performances.

Acknowledgments

The theoretical work was supported by the Consortium des ‘Equipements de Calcul Intensif’ funded by the Fonds National de la Recherche Scientifique (FR-FNRS) under Grant No.2.5020.11. A.R. thanks the ‘Fonds pour la Recherche Industrielle et Agricole’ (FRIA) for his Ph.D. grant. J.C. is an FNRS research director.

References

- [1] Kandel, R. Le réchauffement climatique. Chapter 1: Introduction. *Paris cedex 14 : Presses Universitaires de France*. 2009. 5-14. URL: <https://www.cairn.info/le-rechauffement-climatique--9782130570561-page-5.htm?contenu=resume>
- [2] Kamran, M.; R. Fazal, M. Renewable Energy Conversion Systems. Chapter 1: Fundamentals of renewable energy systems. *Elsevier Inc.* 2021. 1-19.
- [3] Bhawnik, S.; K. Saha, S.; K. Rath, A. New Research Directions in Solar Energy Technologies. Chapter 4: A Perspective on Perovskite Solar Cells. *Energy, Environment, and Sustainability*. Springer, Singapore. 2021. 55-151. DOI: https://doi.org/10.1007/978-981-16-0594-9_4
- [4] Ritchie, H.; Roser, M. Energy mix, Global primary energy: how has the mix changed over centuries? *Our World in Data*. 2022.
- [5] Liu, Z.; Deng, Z.; J. Davis, S. *et al.* Monitoring global carbon emissions in 2021. *Nature reviews earth & environment*. 2022, 3, 217-219. DOI: <https://doi.org/10.1038/s43017-022-00285-w>
- [6] Ritchie, H.; Roser, M. CO₂ emissions, Global CO₂ emissions from fossil fuels. *Our World in Data*. 2022.
- [7] S. Lewis, N.; Crabtree, G., J. Nozik, A. *et al.* Basic Research needs for solar energy utilization, Report on the Basic Energy Sciences Workshop on Solar Energy Utilization. *Argonne National Laboratory*. 2005. 7-10.
- [8] Wang, G. Technology, manufacturing and grid connection of photovoltaic solar cells. Chapter 1: Basic Physics of Solar Cells. *John Wiley & Sons, Singapore*. 2018.
- [9] Labouret, A.; Cumunel, P.; Braun, J-P. *et al.* Cellules solaires, Les bases de l'énergie photovoltaïque. Chapter 3 : Cellules et panneaux photovoltaïques. *Dunod, Paris*. 2010. 31-48.
- [10] Riverola, A.; Vossier, A.; Chemisana, D. Nanomaterials for solar cell applications. Chapter 1: Fundamentals of solar cells. *Elsevier Inc.* 2019. 3-33.
- [11] Amin, N. Comprehensive guide on organic and inorganic solar cells, Fundamental Concepts to Fabrication Methods. Chapter 1: Principle of photovoltaics. *Elsevier Inc.* 2022. 1-23.
- [12] Bhujel, R.; P. Swain, B. Fabrication and characterization of silicon nanowires hybrid Solar cells: a review. *IOP Conference Series: Materials Science and Engineering*. 2018, 377, 012193. DOI: <https://doi.org/10.1088/1757-899X/377/1/012193>
- [13] Abzieher, T.; Mowafak, A-J.; Kirstin, A. *et al.* Best Research-Cell Efficiency Chart. *NREL*. 2022.
- [14] M. Bagher, A. Comparison of organic solar cells and inorganic solar cells. *International Journal of Renewable and Sustainable Energy*. 2014, 3, 53-58. DOI: [10.11648/j.ijrse.20140303.12](https://doi.org/10.11648/j.ijrse.20140303.12)
- [15] Irvine, S. Springer Handbook of Electronic and Photonic Materials. Chapter 46: Solar Cells and Photovoltaics. *Springer Science+Business Media*. 2006. 1095-1106.
- [16] Destruel, P.; Seguy, I. Les cellules photovoltaïques organiques. *Téchniques de l'Ingénieur*. 2004. 25. 1-11.
- [17] Lu, B.; Wang, J.; Zhang, Z. *et al.* Recent progress of Y-series electron acceptors for organic solar cells. *Nano Select*. 2021, 2, 2029-2039. DOI: <https://doi.org/10.1002/nano.202100036>
- [18] Hösel, M.; Angmo, D.; C. Krebs, F. Handbook of organic materials for optical and (opto)electronic devices, Properties and applications. Chapter 17: Organic solar cells (OSCs). *Woodhead Publishing Limited*. 2013. 473-507.
- [19] Wei, Q.; Liu, W.; Leclerc, M. *et al.* A-D-A'-D-A non-fullerene acceptors for high-performance organic solar cells. *Science China Chemistry*. 2020, 63, 1352-1366. DOI: <https://doi.org/10.1007/s11426-020-9799-4>
- [20] Riede, M.; Spoltore, D.; Leo, K. Organic Solar Cells – The Path to Commercial Success. *Advanced Energy Materials*. 2020, 11, 2002653. DOI: <https://doi.org/10.1002/aenm.202002653>
- [21] Hai, J.; Luo, S.; Yu, H. *et al.* Achieving ultra-narrow bandgap non-halogenated non-fullerene acceptor via vinylene -bridges for efficient organic solar cells. *Materials Advances*. 2021, 2, 2132-2140. DOI: <https://doi.org/10.1039/D0MA01017K>
- [22] Uddin, A. Comprehensive guide on organic and inorganic solar cells, Fundamental Concepts to Fabrication Methods. Chapter 2: Organic solar cells. *Elsevier Inc.* 2022. 25-55.
- [23] Wang, K.; Liu, C.; Meng, T. *et al.* Inverted organic photovoltaic cells. *Chemical Society Reviews*. 2016, 45, 2937-2975. DOI: <https://doi.org/10.1039/C5CS00831J>
- [24] Lattante, S. Electron and Hole Transport Layers: Their Use in Inverted Bulk Heterojunction Polymer Solar Cells. *Electronics*. 2014, 3, 132-164. DOI: [10.3390/electronics3010132](https://doi.org/10.3390/electronics3010132)
- [25] D.S. Fung, D.; C.H. Choy, W. Organic Solar Cells, Materials and Device Physics. Chapter 1: Introduction to Organic Solar Cells. *Green Energy and Technology*. Springer-Verlag, London. 2013. 1-16. DOI: [10.1007/978-1-4471-4823-4_1](https://doi.org/10.1007/978-1-4471-4823-4_1)

- [26] Zhao, J.; Yao, C.; Umair Ali, M. *et al.* Recent Advances in High-performance Organic Solar Cells Enabled by Acceptor-Donor-Acceptor-Donor-Acceptor (A-DA'D-A) Type Acceptors. *Materials Chemistry Frontiers*. **2020**, *4*, 3487-3504. DOI: <https://doi.org/10.1039/D0QM00305K>
- [27] Tu, Z.; Han, G.; Yi, Y. Barrier-Free Charge Separation Enabled by Electronic Polarization in High-Efficiency Non-fullerene Organic Solar Cells. *The Journal of Physical Chemistry Letters*. **2020**, *11*, 2585-2591. DOI: <https://doi.org/10.1021/acs.jpclett.0c00405>
- [28] Scharber, M.C.; Sariciftci, N.S. Efficiency of bulk-heterojunction organic solar cells. *Progress in Polymer Science*. **2013**, *38*, 1929-1940. DOI: <https://doi.org/10.1016/j.progpolymsci.2013.05.001>
- [29] Han, G.; Yi, Y. Origin of Photocurrent and Voltage Losses in Organic Solar Cells. *Advanced theory and simulations*. **2019**, *2*, 1900067. DOI: <https://doi.org/10.1002/adts.201900067>
- [30] L. Benanti, T; Venkataraman, D. Organic solar cells: An overview focusing on active layer morphology. *Photosynthesis Research*. **2006**, *87*, 73-81. DOI: <https://doi.org/10.1007/s11120-005-6397-9>
- [31] Xu, B.; Zheng, Z.; Zhao, K. *et al.* A Bifunctional Interlayer Material for Modifying Both the Anode and Cathode in Highly Efficient Polymer Solar Cells. *Advanced Materials*. **2016**, *28*, 434-439. DOI: <https://doi.org/10.1002/adma.201502989>
- [32] H. Park, J.; Lee, T-W.; Chin, B-D. *et al.* Roles of interlayers in efficient organic photovoltaic devices. *Macromol Rapid Commun.* **2010**, *31*, 2095-2108. DOI : <https://doi.org/10.1002/marc.201000310>
- [33] Lai, T-H.; Tsang, S-W.; R. Manders, J. *et al.* Properties of interlayer for organic photovoltaics. *Materials Today*. **2013**, *16*, 424-432. DOI: <https://doi.org/10.1016/j.mattod.2013.10.001>
- [34] Duan, C.; Zhong, C.; Huang, F. *et al.* Organic Solar Cells, Materials and Device Physics. Chapter 3: Interface Engineering for High Performance Bulk-Heterojunction Polymeric Solar Cells. *Green Energy and Technology*. Springer-Verlag, London. **2013**, 1-16. DOI: [10.1007/978-1-4471-4823-4_3](https://doi.org/10.1007/978-1-4471-4823-4_3)
- [35] Yeh, N.; Yeh, P. Organic solar cells: Their developments and potentials. *Renewable and Sustainable Energy Reviews*. **2013**, *21*, 421-431. DOI: <https://doi.org/10.1016/j.rser.2012.12.046>
- [36] Riordan, C.; Hulstron, R. What is an air mass 1.5 spectrum? (solar cell performance calculations). *IEEE Conference on Photovoltaic Specialists*. **1990**, *2*, 1085-1088. DOI: <https://doi.org/10.1109/PVSC.1990.111784>
- [37] Xu, T.; Qiao, Q. Encyclopedia of Nanotechnology. Chapter O: Organic Photovoltaics: Basic Concepts and Device Physics. *Springer, Dordrecht*. **2012**, 2022-2031.
- [38] Kamran, M. Renewable Energy Conversion Systems. Chapter 4: Solar energy. *Elsevier Inc.* **2021**, 109-152.
- [39] Qi, B.; Wang, J. Fill factor in organic solar cells. *Physical Chemistry Chemical Physics*. **2013**, *15*, 8972-8982. DOI: <https://doi.org/10.1039/C3CP51383A>
- [40] Feng, L.; Yuan, J.; Zhang, Z. Thieno[3,2-b]pyrrolo Fused Pentacyclic Benzotriazole Based Acceptor for Efficient Organic Photovoltaics. *ACS Applied Materials and Interfaces*. **2017**, *9*, 31985-31992. DOI: <https://doi.org/10.1021/acsami.7b10995>
- [41] Qiu, D.; A. Adil, M.; Lu, K. *et al.* The Crystallinity Control of Polymer Donor Materials for High Performance Organic Solar Cells. *Frontiers in Chemistry*. **2020**, *8*, 603134. DOI: <https://doi.org/10.3389/fchem.2020.603134>
- [42] Cheng, P.; Li, G.; Zhan, X. *et al.* Next-generation organic photovoltaics based on non-fullerene acceptors. *Nature Photonics*. **2018**, *12*, 131-142. DOI: <https://doi.org/10.1038/s41566-018-0104-9>
- [43] Li, D.; Zhang, X.; Liu, D. *et al.* Aggregation of non-fullerene acceptors in organic solar cells. *Journal of Materials Chemistry A*. **2020**, *8*, 15607-15619. DOI: <https://doi.org/10.1039/D0TA03703F>
- [44] Li, S.; Li, C-Z.; Shi, M. *et al.* New Phase for Organic Solar Cell Researches: Emergence of Y-Series Electron Acceptors and Their Perspectives. *ACS Energy Letters*. **2020**, *5*, 1554-1567. DOI: <https://doi.org/10.1021/acsenergylett.0c00537>
- [45] Kan, B.; Kan, Y.; Zuo, L. *et al.* Recent progress on all-small molecule organic solar cells using small-molecule nonfullerene acceptors. *InfoMat*. **2020**, *3*, 175-200. DOI: <https://doi.org/10.1002/inf2.12163>
- [46] A. Vydrov, O.; E. Scuseria, G. Assessment of a long-range corrected hybrid functional. *The Journal of Chemical Physics*. **2006**, *125*, 234109. DOI: <https://doi.org/10.1063/1.2409292>
- [47] Risko, C.; Brédas, J-L. Multiscale Modelling of Organic and Hybrid Photovoltaics. Chapter 1: Small Optical Gap Molecules and Polymers: Using Theory to Design More Efficient Materials for Organic Photovoltaics. *Springer*. **2013**, 1-38. DOI: https://doi.org/10.1007/128_2013_459
- [48] Chigo-Anota, E.; A. Alejandro, M.; B. Hernández, A. *et al.* Long range corrected-PBE based analysis of the H_2O adsorption on magnetic BC_3 nanosheets. *RSC Advances*. **2016**, *6*, 20409. DOI: [10.1039/c5ra27231a](https://doi.org/10.1039/c5ra27231a)
- [49] Frisch, M.; Trucks, G.; Cheeseman, J. *et al.* Gaussian 16 Rev.A.03 Release Notes. **2017**. URL: https://gaussian.com/relnotes_a03/
- [50] Yuan, J.; Zhang, Y.; Zhou, L. *et al.* Single-Junction Organic Solar Cell with over 15% Efficiency Using Fused-Ring Acceptor with Electron-Deficient Core. *Joule*. **2019**, *3*, 1140-1151. DOI: <https://doi.org/10.1016/j.joule.2019.01.004>
- [51] Cui, Y.; Yao, H.; Zhang, J. *et al.* Over 16% efficiency organic photovoltaic cells enabled by a chlorinated acceptor with increased open-circuit voltages. *Nature Communications*. **2019**, *10*, 2515. DOI: <https://doi.org/10.1038/s41467-019-10351-5>
- [52] Wei, Q.; Yuan, J.; Yi, Y. *et al.* Y6 and its derivatives: molecular design and physical mechanism. *National Science Review*. **2021**, *8*. DOI: <https://doi.org/10.1093/nsr/nwab121>
- [53] Mennucci, B. Polarizable continuum model. *Wires Computational Molecular Science*. **2012**, *2*, 386-404. DOI: [10.1002/wcms.1086](https://doi.org/10.1002/wcms.1086)
- [54] Mennucci, B.; Tomasi, J.; Cammi, R. *et al.* Polarizable Continuum Model (PCM) Calculations of Solvent Effects on Optical Rotations of Chiral Molecules. *The Journal of Physical Chemistry A*. **2002**, *106*, 6102-6113. DOI: [10.1021/jp020124t](https://doi.org/10.1021/jp020124t)
- [55] Lipparini, F.; Scalmani, G.; Mennucci, B. *et al.* Self-Consistent Field and Polarizable Continuum Model: A New Strategy of Solution for the Coupled Equations. *Journal of Chemical Theory and Computation*. **2011**, *7*, 610-617. DOI: <https://doi.org/10.1021/ct1005906>
- [56] Han, G.; Hu, T.; Yi, Y. Reducing the Singlet-Triplet Energy Gap by End-Group Stacking Toward High-Efficiency Organic Photovoltaics. *Advanced Materials*. **2020**, *32*, 2000975. DOI: <https://doi.org/10.1002/adma.202000975>
- [57] Dey, S. Recent Progress in Molecular Design of Fused Ring Electron Acceptors for Organic Solar Cells. *Small*. **2019**, *15*, 1900134. DOI: <https://doi.org/10.1002/smll.201900134>
- [58] Yan, J.; Rodriguez-Martinez, X.; Pearce, D. *et al.* Identifying structure-absorption relationships and predicting absorption strength of non-fullerene acceptors for organic photovoltaics. *Energy & Environmental Science*. **2022**, *15*, 2958. DOI: [10.1039/d2ee00887d](https://doi.org/10.1039/d2ee00887d)
- [59] Londi, G.; Dilmurat, R.; D'Avino, G. *et al.* Comprehensive modelling study of singlet exciton diffusion in donor-acceptor dyads: when small changes in chemical structure matter. *Physical Chemistry Chemical Physics*. **2019**, *21*, 25023-25034. DOI: [10.1039/c9cp05201a](https://doi.org/10.1039/c9cp05201a)
- [60] Yang, J.; Geng, Y.; Li, J. *et al.* A-DA'D-A-Type Non-fullerene Acceptors Containing a Fused Heptacyclic Ring for Poly(3-hexylthiophene)-Based Polymer Solar Cells. *The Journal of Physical Chemistry C*. **2020**, *124*, 24616-24623. DOI: <https://doi.org/10.1021/acs.jpcc.0c07162>
- [61] H. Park, S.; Y. Kwon, N.; J. Kim, H. *et al.* Nonhalogenated Solvent-Processed High-Performance Indoor Photovoltaics Made of New Conjugated Terpolymers with Optimized Monomer Compositions. *ACS Applied Materials & Interfaces*. **2021**, *13*, 13487-13498. DOI: <https://doi.org/10.1021/acsmami.0c22946>
- [62] Picollo, M.; Aceto, M.; Vitorino, T. UV-Vis spectroscopy. *Physical Sciences Reviews*. **2018**, *0*, 1-14. DOI: <https://doi.org/10.1515/psr-2018-0008>
- [63] Itagaki, H. Experimental Methods in Polymer Science - Modern methods in Polymer, Research and Technology. Chapter 3: Fluorescence Spectroscopy. *Elsevier Inc.* **2000**, 155-260. DOI: <https://doi.org/10.1016/B978-0-08-050612-8.50009-X>
- [64] Mahjabin, S.; M. Haque, Md.; Khan, S. *et al.* Effects of oxygen concentration variation on the structural and optical properties of reactive sputtered WO_x thin film. *Solar Energy*. **2021**, *222*, 202-211. DOI: <https://doi.org/10.1016/j.solener.2021.05.031>
- [65] Ma, L.; Xu, Y.; Zu, Y. *et al.* A ternary organic solar cell with 300 nm thick active layer shows over 14% efficiency. *Science China Chemistry*. **2020**, *63*, 21-27. DOI: <https://doi.org/10.1007/s11426-019-9556-7>
- [66] Zhang, S.; Qin, Y.; Zhu, J. *et al.* Over 14% Efficiency in Polymer Solar Cells Enabled by a Chlorinated Polymer Donor. *Advanced Materials*. **2018**, *30*, 1800868. DOI: <https://doi.org/10.1002/adma.201800868>
- [67] Hori, T.; Moritou, H.; Fukuoka, N. *et al.* Photovoltaic Properties in Interpenetrating Heterojunction Organic Solar Cells Utilizing MoO_3 and ZnO Charge Transport Buffer Layers. *Materials*. **2010**, *3*, 4915-4921. DOI: [10.3390/ma3114915](https://doi.org/10.3390/ma3114915)
- [68] Song, J.; Zheng, E.; Wang, X-F. *et al.* Low-temperature-processed ZnO-SnO_2 nanocomposite for efficient planar perovskite solar cells. *Solar Energy Materials & Solar Cells*. **2016**, *144*, 623-630. DOI: <https://doi.org/10.1016/j.solmat.2015.09.054>

Pour vous faire membre de la SRC et accéder gratuitement à la revue Chimie Nouvelle :

il vous suffit de verser au compte BNP Paribas Fortis : BE60 2100 4208 0470
la somme indiquée dans le tableau ci-dessous :

Membres résidant en Belgique et au Luxembourg

Membres effectifs : **50 euros**

- participation gratuite ou à prix réduit à toutes les activités de la SRC
- abonnement gratuit à la revue "Chimie Nouvelle"
- accès gratuit à la bibliothèque de la SRC.

Membres associés : **25 euros**

- réservé, avec les mêmes avantages que les membres effectifs, aux jeunes diplômés du deuxième cycle pendant deux ans, aux professeurs de l'enseignement secondaire et aux retraités.

Membres Juniors : Gratuit

- réservé aux étudiants de dernière année du 2^e cycle universitaire (2^e master), des Ecoles d'Ingénieurs industriels et des gradués en Chimie et Biochimie avec les mêmes avantages que les membres effectifs.

Demandeurs d'emploi : **15 euros**

- mêmes avantages que les membres effectifs + insertion gratuite dans Chimie Nouvelle d'une annonce de demande d'emploi.

Membres résidant à l'étranger

Membres effectifs : **60 euros**

Membres associés : **35 euros**